Theoretical investigation of mixing in warm clouds. Part 2: Homogeneous mixing

M. Pinsky(1), A. Khain(1), A. Korolev(2) and L. Magaritz-Ronen (1)

(1) Department of Atmospheric Sciences, The Hebrew University of Jerusalem, Israel

(2) Environment Canada, Cloud Physics and Severe Weather Section, Toronto, Canada

Submitted to the Atmos. Chem. Phys.

revision (April, 2016)

second revision (May 2016)

Communicating author: Alexander Khain, The Hebrew University of Jerusalem,

alexander.khain@mail.huji.ac.il

Abstract

Evolution of monodisperse and polydisperse droplet size distributions (DSD) during homogeneous mixing is analyzed. Time-dependent universal analytical expressions for supersaturation and liquid water content are derived. For an initial monodisperse DSD, these quantities are shown to depend on a sole non-dimensional parameter. The evolution of moments and moment-related functions in the course of homogeneous evaporation of polydisperse DSD is analyzed using a parcel model.

It is shown that the classic conceptual scheme, according to which homogeneous mixing leads to a decrease in droplet mass at constant droplet concentration, is valid only in cases of monodisperse or initially very narrow polydisperse DSD. In cases of wide polydisperse DSD, mixing and successive evaporation lead to a decrease of both mass and concentration, so the characteristic droplet sizes remain nearly constant. As this feature is typically associated with inhomogeneous mixing, we conclude that in cases of an initially wide DSD at cloud top, homogeneous mixing is nearly indistinguishable from inhomogeneous mixing.

Key words: *turbulent mixing, homogeneous mixing, mono-and polydisperse droplet size distributions*

1. Introduction

Turbulent mixing at cloud edges and cloud tops accompanied by phase transitions has been the focus of numerous studies, beginning with the pioneering works of Baker and Latham (1979), Baker et al. (1980), Blyth et al. (1980) and Baker and Latham (1982). Laboratory experiments by Latham and Reed (1977) showed that after mixing with sub-saturated air some droplets completely evaporate while others remain unchanged. This finding gave rise to the concept of two types of turbulent mixing: homogeneous and inhomogeneous. A recent description of the classical concepts of homogeneous and inhomogeneous mixing can be found in study by Korolev et al. (2016), hereafter referred to as Pt1.

Figure 1 presents a conceptual scheme of homogeneous mixing between saturated cloud volume V_1 containing droplets and sub-saturated droplet-free volume V_2 (Fig. 1a) in case of initially monodisperse droplet size distribution (DSD). This scheme is the base of further analysis. According to the concept of homogeneous mixing, the air within the volumes mixes at a rate much higher than the characteristic rate of droplet evaporation. So, the fields of temperature and humidity (and, therefore, the fields of the relative humidity and supersaturation) are rapidly homogenized throughout the entire volume, and all the droplets experience the same supersaturation (Fig. 1b). At the end of the first stage, the droplet concentration decreases due to dilution down to $N_{m0} = N_1 \frac{V_1}{V_1 + V_2}$, where N_1 is the initial droplet concentration in the cloud volume. At the second stage (Fig. 1c), droplets change supersaturation and temperature through their evaporation. There are two possible scenarios for the final equilibrium states. In the first one, illustrated in Fig. 1c, droplets continue evaporating until they saturate the environment. The size of all droplets decreases, but they evaporate only partially, so the droplet concentration N_{m0} remains unchanged. In the second scenario, when the initially droplet-free volume is very dry,

the droplets penetrated from cloud volume evaporate completely. In case of polydisperse initial DSD, both partial and complete evaporation of droplets determine the final DSD.

In contrast to homogeneous mixing, spatial homogenization during *inhomogeneous* mixing is a relatively slow process. According to the concept of extremely inhomogeneous mixing, some droplets are transported by the turbulent eddies into the dry environment and experience complete evaporation, whereas other droplets remain unchanged. As in the case of homogeneous mixing, the process of droplet evaporation continues until either the environment is saturated or all the droplets evaporate. According to the classical concept, during extremely inhomogeneous mixing the shape of DSD is conserved, however, the total droplet concentration decreases (see review by Devenish et al., 2012 and Pt 1).

The classical concepts analyze only the final equilibrium states which are based on the mass conservation consideration. Strictly speaking, the size distributions in the final states, assumed in the classical concepts, are hypothetical and cannot be reached. This is because the classic concepts do not take into account the mixing-induced DSD broadening. Detailed simulation of time evolution of DSD and other microphysical parameters is necessary not only to better determine the final states, but also to evaluate time periods during which such final states are reached. The analysis of time evolution is practically important because many DSDs measured in-situ correspond to the transient state, but not to the final equilibrium state. Besides, it is necessary to determine the evolution of initially polydisperse DSD, that may substantially differ from the evolution of monodisperse DSD.

We analyze the time evolution of the DSD during homogeneous mixing in cases of monodisperse and polydisperse initial DSDs. The analysis is based on new equations and methodology developed by Pinsky et al. (2013, 2014).

First, we need to evaluate conditions at which mixing can be considered homogeneous. The characteristic spatial scale of homogeneous mixing can be estimated by comparing the

characteristic times of two processes providing thermodynamic equilibrium inside a mixing volume. The first process is mechanical mixing (diffusion) governed by turbulence. Turbulent mixing leads to homogenization of temperature, humidity (and, thus, of supersaturation) as well as of droplet concentration within the volume $V = V_1 + V_2$. The second process is evaporation of a droplet ensemble, which leads to an increase in relative humidity and to the thermodynamical equilibrium in the mixing volume.

The process of mixing that is accompanied by droplet evaporation is characterized by two time scales. The first time scale is the characteristic mixing (homogenization) time τ_{mix} of an entrained volume with linear scale L_{mix} can be evaluated from the relationship (Monin and Yaglom, 1975)

$$\tau_{mix} = \varepsilon^{-1/3} L_{mix}^{2/3} \quad , \qquad (1)$$

where ε is the turbulent kinetic energy dissipation rate. The estimation (1) suggests that the size of the volume falls within the inertial interval of turbulence. Therefore, after the time τ_{mix}, volume with a linear scale of about L_{mix} will be mechanically homogenized and all the droplets in the volume will experience the same supersaturation.

The second time scale characterizes rate of droplet evaporation and corresponding changes of supersaturation. In this study, as well as later in Part.3, it will be shown that the characteristic evaporation time is the *phase relaxation time* τ_{pr}, that determines the rate of change of supersaturation during condensation or evaporation (Mazin, 1968; Korolev and Mazin, 2003)

$$\tau_{pr} = \left(4\pi \mathscr{D} \bar{r} N\right)^{-1}, \qquad (2)$$

where $N = N_{m0}$ is the concentration of droplets in the mixing volume, $\bar{r}$ is the mean radius of droplets and $\mathscr{D}$ is the diffusivity of water vapor. The spatial scale at which the mixing time is

equal to the phase relaxation time is called a phase relaxation scale L_{pr} (Mazin, 1968). This scale can be calculated from Eqs. (1) and (2) as

$$L_{pr} = \varepsilon^{1/2}\tau_{pr}^{3/2} \approx \varepsilon^{1/2}\left(4\pi\mathscr{D}\bar{r}N\right)^{-3/2} \quad (3)$$

The type of mixing is often characterized by the value of the Damköhler number which in regard to atmospheric mixing is defined as the ratio τ_{mix}/τ_{pr} (Baker et al., 1980; Jeffery, 2007; Lehmann et al., 2009):

$$Da = \frac{\tau_{mix}}{\tau_{pr}} = \frac{4\pi\mathscr{D}\bar{r}NL_{mix}^{2/3}}{\varepsilon^{1/3}} \quad (4)$$

The case $Da << 1$ corresponds to homogeneous mixing, when mechanical homogenization occurs much faster than does droplet evaporation. The case $Da >> 1$ corresponds to extremely inhomogeneous mixing. It is reasonable to consider the value $Da = 1$ as a boundary separating the two types of mixing. This condition is equivalent to the condition

$$L_{mix} = L_{pr} \approx \varepsilon^{1/2}\left(4\pi\mathscr{D}\bar{r}N\right)^{-3/2} \quad (5)$$

Expression (5) determines the maximum spatial scale at which mixing can be considered as homogeneous. The evaluation of the spatial scales at conditions typical of different cloud types is presented in **Table 1**. One can see that the characteristic volume size at which mixing can be considered homogeneous ranges from 0.2 m to 0.6 m. At larger scales, supersaturation within the mixing volume is non-uniform and droplets in the volume experience different values of relative humidity. In this case, the mixing should be considered inhomogeneous.

The further paper structure is the following. In Section 2 we calculate the thermodynamic characteristics of the resulting volume at the end of the first stage of mixing (see Fig. 1b).

144 Section 3 presents an analytic solution of homogeneous droplet evaporation in the monodisperse
145 DSD case. In Section 4 effects of polydispersivity on the DSD evolution are described. The
146 problem of turbulent mixing representation in numerical cloud models is discussed in Section 5.
147 The main results of the study are presented in Conclusion Section 6.
148

149 **2. Thermodynamic characteristics of the mixing volume at the end of the first stage**

150 At the first stage (see the scheme in Fig.1) homogeneous mixing is considered as an isobaric
151 process that is not accompanied by phase transitions (Korolev and Isaac, 2000). Let us consider
152 mixing between a cloud volume with mass m_1, supersaturation $S_1 = 0$ and temperature T_1 and a
153 droplet-free volume with mass m_2, supersaturation $S_2 < 0$ and temperature T_2. The cloud
154 volume also contains droplets with concentration N_1 and liquid water mixing ratio q_1 (Fig. 1).
155 For the sake of simplicity, we assume that the mass of both volumes is equal to one. Let us
156 further assume that μ is the mass fraction of the cloud air that mixes with the mass fraction
157 $(1-\mu)$ of the droplet-free air. In this case, the air mass in the mixing volume will be equal to
158 $m_1\mu + (1-\mu)m_2 = 1$. Isobaric mixing leads to an approximate linear dependence of droplet
159 concentration N_{m0} on μ.

160 After an instantaneous homogenization of the two volumes, the intermediate temperature
161 T_{m0}, droplet concentration N_{m0} and liquid mixing ratio q_{m0} are (see Pt.1):

162 $$N_{m0} = N_1\mu; \quad q_{m0} = q_1\mu; \quad T_0 = T_1\mu + T_2(1-\mu) \qquad (6a)$$

163 If the temperature difference $|T_1 - T_2|$ does not exceed a few degrees, the intermediate
164 supersaturation S_{m0} can be approximated by a linear dependence on μ

165 $$S_{m0} = S_2(1-\mu) \qquad (6b)$$

166 **Figure 2** shows, that in case $|T_1 - T_2| < 2^{o}C$, the deviations of supersaturation from the linear
167 dependence (6b) are small enough and can be neglected. In cases when the temperature of the
168 dry volume substantially differs from the temperature of the cloud volume, the dependence of the
169 resulting supersaturation on parameter μ becomes non-linear (Fig. 2). At temperature
170 differences of 5-10 ^{o}C, the deviation from the analytical solution (6) increases, which requires
171 using more precise formulas for supersaturation (see Pt. 1). Values of N_{m0}, q_{m0}, T_{m0} and S_{m0}
172 determine the initial conditions for the second stage of homogeneous mixing. This is actually
173 homogeneous evaporation of droplets, which leads to a thermodynamic equilibrium between
174 water vapor and liquid water.
175
176 **3. Analysis of homogeneous droplet evaporation in the monodisperse DSD case**
177
178 **3.1. Basic assumptions and equations**
179 The second stage of mixing consists in homogeneous evaporation of droplets. The evolution
180 of DSD during the second stage is considered here under the following assumptions: a) the
181 processes inside the mixing volume are adiabatic, b) the droplet size distribution is
182 monodisperse, c) the vertical velocity of the volume $u_z = 0$ and d) the sedimentation of droplets
183 is neglected and their concentration remains constant.
184 The liquid water mixing ratio can be expressed as
185 $$q(t) = \frac{4\pi\rho_w}{3\rho_a} N r^3(t) \qquad (7)$$
186
187 where $r(t)$ is the radius of droplets and N is the droplet number concentration. Closed
188 equations describing condensation/evaporation in a moving adiabatic air volume were obtained

189 by Pinsky et al. (2013). In an unmoving adiabatic volume, evaporation is described by the
190 equation for supersaturation (e.g., Korolev and Mazin, 2003)

191 $$\frac{1}{S+1}\frac{dS}{dt} = -A_2\frac{dq}{dt} \qquad (8)$$

192 and droplet evaporation is described by the simplified equation (Pruppacher and Klett, 2007)

193 $$r\frac{dr}{dt} = \frac{S}{F}, \qquad (9)$$

194 where S is the supersaturation over a flat water surface. For cloud droplets Eq. (9) is valid with
195 high accuracy. We do take into account formation of haze particles resulting from droplet
196 evaporation. This allows us to neglect the curvature term and chemical term in the evaporation
197 equation. Coefficients A_2 and F in Eqs. (8, 9) are slightly dependent on the temperature and the
198 pressure

199 $$A_2 = \frac{1}{q_v} + \frac{L^2}{c_p R_v T^2} \qquad (10)$$

200 $$F = \frac{\rho_w L^2}{k_a R_v T^2} + \frac{\rho_w R_v T}{e_S(T)\mathscr{D}} \qquad (11)$$

201 We assume that coefficients A_2 and F do not change in the course of droplet evaporation.
202 The physical meaning and units of other variables are given in **Appendix A.**
203

204 **3.2. Time evolution of supersaturation and of liquid water content**

205 The closed differential equations for the liquid water mixing ratio q and supersaturation S
206 to be used in the analysis are derived in **Appendix B.**

207 $$\frac{dq}{dt} = BN_{m0}^{2/3}\left[(S_{m0}+1)\exp\{-A_2(q-q_{m0})\}-1\right]q^{1/3} \qquad (12)$$

208 $$\frac{1}{S+1}\frac{dS}{dt} = -A_2 BN_{m0}^{2/3} S\left(q_{m0} - \frac{1}{A_2}\ln\frac{S+1}{S_{m0}+1}\right)^{1/3} \qquad (13)$$

where

$$B = \frac{3}{F}\left(\frac{4\pi\rho_w}{3\rho_a}\right)^{2/3} = const \qquad (14)$$

The solutions of these equations depend on the values of N_{m0}, q_{m0}, T_{m0}, and S_{m0}, obtained after the first stage of mixing. Eqs. (12) and (13) are rigidly connected by the following equation directly following from Eq. (8):

$$\ln[S(t)+1] = -A_2 q(t) + C \qquad (15)$$

where $C = \ln[S_{m0}+1] + A_2 q_{m0}$ is determined by the initial conditions at $t = 0$.

Since in this study we assume $S(t) \le 0$, it is convenient to use the relative humidity RH and the saturation deficit SD to characterize the thermodynamic state of the mixing volume. Both quantities are easily related to $S(t)$: $SD(t) = -S(t)$, $RH(t) = 1 + S(t)$. **Figure 3** demonstrates dependencies $S(t)$ and $q(t)$, calculated at an initial relative humidity RH_0 that varies from 72% to 91.6%, and an initial LWC of 0.6 gm^{-3}. RH_{m0} corresponds to the relative humidity in dry volume RH_2, that ranges from 43% to 83% at $\mu = 0.5$. The results of solving Eqs. (14-15) were compared with those obtained using a parcel model (Korolev, 1995) in which evaporation is described using equations with temperature-dependent parameters, and were found to be in excellent agreement. This agreement can be attributed to the fact that temperature changes that occurred in the course of the mixing are relatively small, validating the assumption about the constancy of A_2 and F.

As seen from Fig. 3, the final equilibrium state may be reached within several seconds. Fig. 3 shows the possibility of the two final states mentioned above: a) complete droplet evaporation

reached at different time instances depending on the initial value of S_{m0}, and b) partial droplet evaporation at $RH_{m0} > 82\%$. In the latter case, the final supersaturation is equal to zero.

3.3. Universal dependencies of supersaturation and of LWC on time

In order to simplify the further analysis we introduce the following non-dimensional parameters: normalized liquid water mixing ratio $\tilde{q} = \frac{q}{q_{m0}}$ which is equal to normalized liquid water content, normalized supersaturation $\tilde{S} = \frac{S}{A_2 q_{m0}}$, and non-dimensional time $t = t/\tau_{m0}$, where $\tau_{m0} = \left(BA_2 N_{m0}^{2/3} q_{m0}^{1/3}\right)^{-1}$ is the time scale. Then the set of non-dimensional equations describing changes of supersaturation and liquid mixing ratio can be written as (see Appendix B for detail)

$$\tilde{S}(\tilde{t}) = -\tilde{q}(\tilde{t}) + \gamma \tag{16}$$

$$\frac{d\tilde{q}}{d\tilde{t}} = \tilde{q}^{1/3}\left(\gamma - \tilde{q}\right) \tag{17}$$

$$\frac{d\tilde{S}}{d\tilde{t}} = -(\gamma - \tilde{S})^{1/3}\tilde{S}, \tag{18}$$

where

$$\gamma = 1 + \frac{S_{m0}}{A_2 q_{m0}} = 1 + \frac{1-\mu}{\mu}\frac{S_2}{A_2 q_1} \tag{19}$$

is dimensionless parameter which depends on the initial supersaturation S_{m0} and the initial liquid water mixing ratio q_{m0}. The value of this parameter can be either positive or negative. Eqs. (16-18) are strictly valid if $|S_{m0}| << 1$, i.e. when the value of supersaturation S is negligible in comparison with unity in the factor $(S+1)^{-1}$ on the left-hand side of Eq. (8). However, a detailed comparison of solutions of Eqs. (16-18) with those obtained using a numerical model showed

that Eqs. (16-18) provide accurate solution at RH_{m0} as low as 30-40%. Eq. (17) should be solved with the initial condition $\tilde{q}(0)=1$, and Eq. (18) should be solved with the initial condition $\tilde{S}(0)=\dfrac{S_{m0}}{A_2 q_{m0}}<0$. Therefore, solutions of both equations depend on the sole parameter γ. Eqs. (17) and (18) are rigidly connected by balance equation Eq. (16).

Defining $x(\tilde{t})=\left(\tilde{q}(\tilde{t})\right)^{1/3}$ and $\chi=|\gamma|^{1/3}\mathrm{sgn}(\gamma)$, the solution of Eq. (17) with the initial condition $x(0)=1$ is

$$2\chi\tilde{t}=\ln\left[\frac{(1-\chi)^2}{(x-\chi)^2}\frac{x^2+\chi x+\chi^2}{1+\chi+\chi^2}\right]+2\sqrt{3}\left[\operatorname{atan}\frac{2\sqrt{3}\chi(1-x)}{3\chi^2+(2+\chi)(2x+\chi)}\right] \qquad (20)$$

The solution for the normalized supersaturation can be obtained from Eq. (20) and the balance equation (16)

$$\tilde{S}(\tilde{t})=-\tilde{q}(\tilde{t})+\gamma=-x^3(\tilde{t})+\chi^3 \qquad (21)$$

Figure 4 demonstrates time dependencies $\tilde{S}(\tilde{t})$ and $\tilde{q}(\tilde{t})$ calculated at different γ at $S_{m0}>-10\%$ (i.e. $RH_{m0}>90\%$). As seen from Fig. 4. the analytical solution is quite close to the numerical one. The deviation increases with a decrease in parameter γ. At $\gamma=-0.5$, the error in the final *RH* is about 15%. The initial RH_{m0} in this case is about 90 %. RH_{m0} is the relative humidity in the mixing volume V after the first stage of mixing. As mentioned above, RH_{m0} may be substantially higher than RH_2 in the initially droplet-free volume. *In-situ* measurements (Gerber et al., 2008) and remote measurements of aerosol humidification (Knight and Miller, 1998; Bar-Or et al., 2012) indicate the existence of zones of high *RH* along cloud edges. These observations and results of numerical simulations indicate that the analytical solution (20-21) is a universal one and applicable at any RH values in cloud surrounding.

The amplitude of the deviation of the analytical solution for supersaturation from the modeled result decreases with the decrease of γ. The cause of the deviation is neglecting term $(S+1)$ on the left-hand side of Eq. (8).

There are two types of solutions determined by parameter χ (or parameter γ), separated by value $\chi = 0$ (Figs. 3 and 4). Condition $\chi = 0$ corresponds to $\mu = \mu_{cr}$ (see Pt 1) and indicates complete evaporation of all the droplets and the relative humidity increasing up to 100 %. Condition $\chi > 0$ corresponds to solutions $\tilde{q}(\tilde{t})$ with asymptotic behavior at $\tilde{t} \to \infty$: $\tilde{q} \to \gamma$ and $\tilde{S} \to 0$, which means that droplets do not completely evaporate. Condition $\chi < 0$ means that all the droplets completely evaporate.

At $\chi = 0$, the analytical solution is:

$$x = \frac{3}{\tilde{t}+3}; \quad \tilde{q}(\tilde{t}) = \left(\frac{3}{\tilde{t}+3}\right)^3; \quad \tilde{S}(\tilde{t}) = -\left(\frac{3}{\tilde{t}+3}\right)^3 \tag{22}$$

Both LWC and supersaturation tend to zero at $\tilde{t} \to \infty$.

At $\chi < 0$, the duration of the evaporation is limited in time (Figs. 3, 4). Normalized evaporation time t_e depends on parameter χ only. This dependence can be obtained from Eq. (20) at $x = 0$:

$$t_e = \frac{1}{2\chi} \ln \frac{(1-\chi)^2}{1+\chi+\chi^2} + \frac{\sqrt{3}}{\chi} \operatorname{atan} \frac{\sqrt{3}}{2\chi+1} \tag{23}$$

Here the time is counted in the relaxation time scales. This fact indicates that the phase relaxation time is the time scale that should be used in the analysis of mixing. The choice of a time scale will be discussed elaborated in greater detail below.

290 At $\chi > -1/2$, one have to use the values $\operatorname{atan}\left(\frac{\sqrt{3}}{2\chi+1}\right)-\pi$ in Eq. (23) instead of $\operatorname{atan}\frac{\sqrt{3}}{2\chi+1}$.

291 t_e is the time needed for supersaturation to reach its maximal value (Figs. 3a, 4a). This value is

292 calculated from Eqs. (16) and (6)

293 $$\tilde{S}_{\max} = \gamma = \chi^3 = 1 + \frac{S_{m0}}{A_2 q_{m0}} \approx 1 + \frac{S_2}{A_2 q_1}\frac{1-\mu}{\mu} = 1 + R\frac{1-\mu}{\mu} \qquad (24)$$

294 where $R = \frac{S_2}{A_2 q_1}$ is a dimensionless parameter describing the ratio of S_2 in the initially dry air

295 and the reserve of liquid water available for evaporation. (This parameter can be determined

296 more precisely using Eq. (2) or Eq. (4) given in Pt. 1). This parameter can be referred to as a

297 potential evaporation parameter (PEP). The PEP is proportional to the ratio of the amount of

298 water vapour that should evaporate in order to saturate the initially droplet-free volume (that is

299 determined by S_2) to the initial available liquid water q_1 in the cloud volume in case of equal

300 initial volumes $V_1 = V_2$.

301 The dependence $t_e(\chi)$ is shown in **Figure 5. O**ne can see that at large sub-saturation values

302 ($\chi < -0.4$) all the droplets evaporate within the span of a few relaxation times, and the analytical

303 results agree well with the model (benchmark) results. At a high initial *RH*, droplet evaporation

304 increases the humidity to nearly the saturation value, at which evaporation becomes extremely

305 slow. In this case, simplified analytical formulas overestimate the evaporation time.

306 At $\chi > 0$, droplets partially evaporate, q reaches the minimal value and the thermodynamic

307 equilibrium is reached when $S \to 0$. Minimal normalized equilibrium LWC can be found from

308 Eqs. (21) and (6)

309 $$\tilde{q}_{\min} = \gamma = \chi^3 = 1 + R\frac{1-\mu}{\mu} \qquad (25)$$

310 Eq. (25) is similar to Eqs. (4-5) (see Pt.1.).

Dependences of $\tilde{S}_{\max}$ and $\tilde{q}_{\min}$ on cloud air fraction, calculated at different initial conditions using Eqs. (24) and (25) are shown in **Figure 6**. The diagram in Fig. 6b is actually a kind of widely used mixing diagram for homogeneous mixing, and Eq. (25) is an universal analytic equation for calculation of this diagram depending on the non-dimensional parameter R. Panel (a) shows that the higher the cloud fraction of air parcels involved in mixing, the lower the saturation deficit, i.e. the higher the final *RH* is. At small R, saturation is reached at a low μ. Similar diagrams in physical units are shown in Pt.1 in Figs. 4a,g.

The equations presented above allow to predict the results of homogeneous mixing both for partial and complete evaporation of droplets (**Table 2)**. One can see that at low temperatures, the environment air volume becomes cloudy at relatively low values of liquid water content in the cloud volume even if *RH* of the environment volume is as low as 50%. The reason is that the saturation ratio at low temperatures is low and only a small amount of liquid should be evaporated to make the initially dry volume saturated.

The diagram in Fig.6b allows to calculate the final liquid water content remaining in the entire volume after saturation reaches 100%. This diagram also shows that for each value of μ there is a certain value of R at which full evaporation takes place. The remaining $\tilde{q}_{\min}$ increases with decreasing q_1 and increasing RH_2, as shown by the arrow.

The natural time scale of the evaporation and, therefore, homogeneous mixing was determined as $\tau_{m0} = \left(BA_2 {N_{m0}}^{2/3} q_{m0}^{1/3}\right)^{-1}$. This value is inversely proportional to $N_{m0} r_{m0}$ and actually coincides with the initial phase relaxation time τ_{pr}. The equality of the characteristic time scales of variations in supersaturation and in liquid water content directly follows from the equation (15). Indeed, in case of $|S| << 1$ the equation can be rewritten as $S(t) = -A_2 q(t) + C$ thus establishing a linear relationship between the supersaturation and the liquid water mixing ratio.

334 It should be emphasized that τ_{m0} is not the time of total droplet evaporation or the time of
335 reaching saturation (when evaporation is over). The time of complete evaporation of all droplets
336 can be substantially longer than phase relaxation time τ_{m0}.

337

338 **4. Analysis of homogeneous droplet evaporation in case of a polydisperse DSD**

339 **4.1. DSD evolution in the course of droplet evaporation**

340 To analyse polydisperse DSD evolution during droplet evaporation at the second stage of
341 homogeneous mixing, we use the same equations for diffusional growth (9) and supersaturation
342 (8) as those used in case of a monodisperse DSD. The solution of Eq. (9) can be written in the
343 form

344 $$r^2(t) = r_0^2 - Q(t) \qquad (26)$$

345 where the non-negative function $Q(t) \geq 0$ is proportional to the supersaturation integral

346 $$Q(t) = -\frac{2}{F}\int_0^t S(t')dt' \geq 0 \qquad (27)$$

347 This function characterizes a decrease in the square of droplet radii. At $t = 0$, $Q(0) = 0$. Let
348 $f_0(r_0)$ be an initial DSD immediately following the first stage of homogeneous mixing. This
349 distribution obeys the normalization condition

350 $$N_{m0} = \int_0^\infty f_0(r_0)dr_0 \qquad (28)$$

351 where N_{m0} is the initial droplet number concentration after the first stage of mixing. Using the
352 inverse transformation $r_0 = \sqrt{r^2 + Q(t)}$ alongside with condition $r \geq 0$ and the relation between
353 the distribution functions $f(r,t) = f_0(r_0)\frac{dr_0}{dr}$ we get

$$f(r,t)=\begin{cases}\dfrac{r}{\sqrt{r^2+Q(t)}}\,f_0\left(\sqrt{r^2+Q(t)}\right), & r\ge 0\\ 0, & r<0\end{cases} \tag{29}$$

Eq. (29) shows that the time changes in DSD and in its moments depend both on the initial DSD at $t=0$, $f_0(r_0)$ and on the time-dependent function $Q(t)\ge 0$.

To illustrate the DSD evolution using Eq. (29), we assume that the initial distribution immediately following the first stage of mixing can be represented by a Gamma distribution:

$$f_0(r_0)=\frac{N_{m0}}{\Gamma(\alpha)\beta}\left(\frac{r_0}{\beta}\right)^{\alpha-1}\exp\left(-\frac{r_0}{\beta}\right) \tag{30}$$

where N_{m0} is an intercept parameter, α is a shape parameter and β is a slope parameter of distribution. Different sets of parameters allow approximations of both narrow and wide DSD. The parameters of the initial Gamma distribution used in this study are presented in **Table 3** and are chosen so that the modal radii of DSD and the LWC would be the same for both distributions.

Combining Eqs. (29) and (30) yields an equation for DSD evolution as a function of $Q(t)$

$$f(r,t)=\begin{cases}\dfrac{N_{m0}}{\Gamma(\alpha)\beta^{\alpha}}(r^2+Q)^{\frac{\alpha}{2}-1}\,r\exp\left(-\dfrac{\sqrt{r^2+Q}}{\beta}\right), & r\ge 0\\ 0, & r<0\end{cases} \tag{31}$$

This DSD (31) depends on four parameters, wherein parameter $Q(t)$ increases with time according to Eq. (27). Examples of evolutions of an initially narrow DSD and an initially wide DSD are shown in **Figure 7**. All the calculations were performed using a parcel model (Korolev, 1995).

There is a significant difference between evolution of DSDs in cases of monodisperse and polydisperse DSDs. At a monodisperse DSD, droplet concentration remains unchanged until the final stage of evaporation when droplets become small and then all evaporate rapidly. At a

polydisperse DSD the droplet concentration decreases simultaneously with the decrease in LWC. Evaporation of a the narrow size distribution is consistent with the concept of homogeneous mixing (Fig. 7a). However homogeneous evaporation of droplets with a wide DSD may be mistakenly taken for inhomogeneous mixing.

4.2. Evolution of DSD moments and related functions

Eq. (29) also allows evaluation of droplet concentration, DSD moments and related functions. Droplet concentration corresponds to the zero moment of DSD and can be expressed as

$$N(t)=\int_0^\infty f(r,t)dr=\int_0^\infty \frac{r}{\sqrt{r^2+Q(t)}}\, f_0\left(\sqrt{r^2+Q(t)}\right)dr=\int_{\sqrt{Q(t)}}^\infty f_0(r_0)dr_0 \qquad (32)$$

Since function $Q(t)$ monotonically increases with the time, the right-hand integral in Eq. (32) decreases, indicating a decrease in droplet concentration with time. If the initial distribution of droplets is described by a Gamma distribution, the decrease of droplet concentration with the time is evaluated using Eqs. (30) and (32) as

$$N(t)=\int_{\sqrt{Q(t)}}^\infty f_0(r_0,t)dr_0=\int_{\sqrt{Q(t)}}^\infty \frac{N_{m0}}{\Gamma(\alpha)\beta}\left(\frac{r_0}{\beta}\right)^{\alpha-1}\exp\left(-\frac{r_0}{\beta}\right)dr_0=$$

$$\frac{N_{m0}}{\Gamma(\alpha)}\int_{\frac{\sqrt{Q(t)}}{\beta}}^\infty x^{\alpha-1}\exp(-x)dx=N_{m0}\frac{\Gamma(\alpha,\eta)}{\Gamma(\alpha)}. \qquad (33)$$

where

$$\eta(t)=\frac{\sqrt{Q(t)}}{\beta} \qquad (34)$$

is a non-dimensional function of time and $\Gamma(\alpha,\eta(t))$ is an upper incomplete Gamma function (Korn and Korn, 2000). It follows from Eqs. (32) and (33) that $N(t)\le N_0$. The dependencies of

395 the normalized droplet concentration $\frac{N(t)}{N_{m0}}$ on time for an initially narrow DSD and an initially

396 wide DSD are shown in **Figure 8**.

397 Fig. 8 shows that in case of an initially narrow DSD, droplet concentration does not change

398 during the first 20 s when $RH_0 = 91.6\ \%$ because the DSD does not shift strongly enough

399 toward smaller droplet radii. At lower initial supersaturations, droplet concentration decreases

400 with time. This decrease may take place rapidly and may last several seconds only. The red line

401 separates two different evaporation scenarios. The curves above the red line correspond to partial

402 evaporation and reaching the saturation state, whereas the curves below the red line correspond

403 to complete evaporation of droplets and the environment remains subsaturated.

404 At an initially wide DSD, droplet concentration decreases at any initial subsaturation value

405 because the DSD contains small droplets that start evaporating regardless the subsaturation

406 value. In the particular example shown in Fig. 8, the droplet relaxation time is shorter in case of a

407 wide DSD, so droplet concentration decreases slower than at a narrow DSD. Droplet

408 concentration decreases substantially during a few tens of seconds, but does not reach zero due

409 to a significant concentration of large droplets in the wide DSD. The equilibrium state is not

410 reached within 20 s.

411 Fig. 8 also demonstrates an excellent agreement between the results of analytical calculations

412 performed using Eq. (33) and results obtained using the parcel model.

413 A normalized moment of the *k-th* order is evaluated as

414
$$\overline{r^k(t)} = \frac{1}{N(t)}\int_0^\infty r^k f(r,t)dr = \frac{1}{N(t)}\int_0^\infty \frac{r^{k+1}}{\sqrt{r^2+Q(t)}} f_0\left(\sqrt{r^2+Q(t)}\right)dr = \frac{1}{N(t)}\int_{\sqrt{Q(t)}}^\infty \left(r_0^2 - Q(t)\right)^{k/2} f_0(r_0)dr_0$$

415

$$\overline{r^k}(t) = \frac{\int_{\sqrt{Q(t)}}^{\infty} \left(r_0^2 - Q(t)\right)^{k/2} f_0(r_0) dr_0}{\int_{\sqrt{Q(t)}}^{\infty} f_0(r_0) dr_0} \qquad (35)$$

In case when the initial distribution is given by the Gamma distribution (30), Eq. (35) leads to the following equation

$$\overline{r^k}(t) = \frac{\beta^k}{\Gamma\left(\alpha, \eta(t)\right)} \int_{\eta(t)}^{\infty} \left(x^2 - \eta^2(t)\right)^{k/2} \left(x\right)^{\alpha-1} \exp\left(-x\right) dx \qquad (36)$$

The even moments can be represented using incomplete the Gamma functions.

Figures 9 and 10 show the time dependencies of quantities typically used for characterizing the DSD shape, namely the mean radius $\overline{r}(t)$ (panel (a)), the effective radius $r_{eff}(t) = \frac{\overline{r^3}(t)}{\overline{r^2}(t)}$ (panel (b)), the RMS width of DSD $\sigma(t) = \sqrt{\overline{r^2}(t) - \overline{r}^2(t)}$ (panel (c)) and the dispersion coefficient $\delta(t) = \frac{\sigma(t)}{\overline{r}(t)}$ (panel (d)). The dependencies corresponding to an initially narrow DSD are shown in Fig. 9 and those corresponding to an initially wide DSD are shown in Fig. 10.

At an initially narrow DSD, the mean radius and the effective radius decrease with time in agreement with the concept of homogeneous mixing. Formation of plateaus in the mean radii, in the effective radii and in droplet dispersion over long time periods is caused by the existence of droplets in the tail of DSD distributions. While the concentration of such droplets is negligibly small, their evaporation takes a significant amount of time.

At an initially wide DSD (Fig.7b), complete evaporation of the smallest droplets starts at the very beginning of the second stage of mixing. This evaporation leads to an increase in the effective radius and in the mean radius that changes non-monotonically. An increase in the value of the effective radius contradicts the concept of homogeneous mixing, according to which both the mean radii and the effective radii decrease in the course of mixing. This increase is

436 explained by the fact that subsaturation at an initially wide DSD leads to a significant rapid
437 decrease in the concentration of small droplets, while the changes in LWC whose value is
438 determined by larger droplets, do not occur that quickly.

439 The opposite behaviors of the effective radii (as well as of the other characteristic droplet
440 sizes) at a narrow DSD vs. a wide DSD, illustrated in Figs. 9 and 10, suggest the existence of a
441 large number of DSDs with initial shapes at which the evaporation of droplets leads to a decrease
442 in droplet concentration, but does not change significantly the effective radius. So the constancy
443 of the effective radius at varying droplet concentrations does not allow to distinguish the mixing
444 type with full confidence. Even at a narrow DSD, the decrease in the value of the effective radius
445 does not exceed 20% at the an initial saturation deficit of 8.4 %.

446 In any case the evolution of DSD and of their parameters is determined by the competition
447 between two effects. First, this is the effect of partial droplet evaporation which shifts the DSD
448 toward smaller sizes and leads to a decrease in the mean radii and in the effective radii, as well
449 as widens the DSD. Second, this is the effect of complete evaporation of the smallest droplets,
450 which increases both the mean radii and the effective radii. The relative contribution of these two
451 effects depends on the initial DSD width and the value of the mean radius. The best indicators of
452 these two effects are the DSD width, σ and the DSD dispersion $\frac{\sigma}{\overline{r}}$.

453 At an initially narrow DSD and an initially low *RH*, partial evaporation initially dominates
454 and the DSD width increases due to the appearance of smaller droplets (Fig. 9c). Afterwards,
455 when complete droplet evaporation becomes the dominant factor, the DSD shifts significantly to
456 small sizes and the DSD width decreases. At an initially large *RH*, complete droplet evaporation
457 is not efficient, and the DSD gets continuously wider. Since the mean radius decreases, the DSD
458 dispersion tends to constant values at any initial *RH*. However, the largest DSD dispersion takes
459 place at an initially low *RH*, when evaporation substantially decreases the mean droplet radius.

460 As seen in Figs. 9d and 10d, the initial DSD dispersion at a narrow DSD is 0.1, while the initial
461 dispersion at a wide DSD is 0.5.

462 Figs. 10c and 10d show that at an initially wide DSD, homogeneous evaporation leads to an
463 increase in both DSD width and DSD dispersion. The increase in the DSD width indicates that
464 formation of the smallest droplets by partial evaporation is the main mechanism of the DSD
465 shape evolution. The DSD dispersion increases with time and rapidly reaches quasi-stationary
466 values of about 0.56 that are typical of real clouds.

467

468 **4.3. Evolution of LWC and of supersaturation**

469 Using Eq. (35), the time dependence of the liquid water mixing ratio is represented as

470 $$q(t)=\frac{4\pi\rho_w}{3\rho_a}N(t)\overline{r^3(t)}=\frac{4\pi\rho_w}{3\rho_a}\int\limits_{\sqrt{Q(t)}}^{\infty}\left(r_0^2-Q(t)\right)^{3/2}f_0(r_0)dr_0 \qquad (37)$$

471 If the initial DSD is approximated by a Gamma distribution, $q(t)$ can be written as

472 $$q(t)=\frac{4\pi\rho_w}{3\rho_a}\int\limits_{\sqrt{Q(t)}}^{\infty}\left(r_0^2-Q(t)\right)^{3/2}\frac{N_{m0}}{\Gamma(\alpha)\beta}\left(\frac{r_0}{\beta}\right)^{\alpha-1}\exp\left(-\frac{r_0}{\beta}\right)dr_0=$$
$$\frac{4\pi\rho_w}{3\rho_a}\frac{N_{m0}\beta^3}{\Gamma(\alpha)}\int\limits_{\eta(t)}^{\infty}\left(x^2-\eta^2(t)\right)^{3/2}\left(x\right)^{\alpha-1}\exp\left(-x\right)dx \qquad (38)$$

473 Since at $t=0$, $\eta=0$ and the initial liquid water mixing ratio is equal to
474 $q_{m0}=\frac{4\pi\rho_w}{3\rho_a}N_{m0}\beta^3\frac{\Gamma(\alpha+3)}{\Gamma(\alpha)}$, hence the normalized liquid water mixing ratio is calculated as

475 $$\frac{q(t)}{q_{m0}}=\frac{1}{\Gamma(\alpha+3)}\int\limits_{\eta(t)}^{\infty}\left(x^2-\eta^2(t)\right)^{3/2}\left(x\right)^{\alpha-1}\exp\left(-x\right)dx \qquad (39)$$

476

477 **Figure 11** shows the time dependencies of LWC for different initial RH_0 in the resulting
478 volume (Fig.11a: an initially narrow DSD; Fig.11b: an initially wide DSD). One can see that at
479 an initially narrow DSD the LWC rapidly decreases, either to zero (full evaporation) or, as in the

480 monodisperse case, to an equilibrium value during a time period of the phase relaxation time (see
481 Section 3 for comparison). At an initially wide DSD, the LWC decreases slowly and
482 monotonically. In general, at an initially narrow DSDs the time dependencies, $q_w(t)$ are quite
483 close to those for monodisperse DSD (Fig. 3b). The higher the initial *RH*, the smaller the change
484 in the LWC is.

485 To calculate the time dependencies of supersaturation, one can use the full equation (8) or
486 Eq. (15) written in the form:

487 $$S(t) = (S_{m0} + 1)\exp\left\{-A_2\left[q(t) - q_{m0}\right]\right\} - 1 \qquad (40)$$

488 In Eq. (40), S_{m0} and q_{m0} are the initial supersaturation and the liquid water mixing ratio,
489 respectively, at $t = 0$. The corresponding time dependencies are shown in **Figure 12.** The
490 analytical results of Eq. (40) are compared with the exact numerical solution obtained by a parcel
491 model, showing a good agreement. The behavior of supersaturation at a initially narrow DSD is
492 similar to that of a monodisperse DSD (Fig. 3a). As in Fig. 3a, the equilibrium non-zero values
493 of subsaturation correspond to complete droplet evaporation. At initially wide DSD, the
494 saturation deficit monotonically decreases as a consequence of the monotonic decrease in the
495 LWC.

496 **Figure 13** shows the dependencies of normalized LWC on normalized droplets
497 concentrations calculated at different values of the initial relative humidity RH_{m0} in the mixing
498 volume ((a): the initially narrow DSD and (b) the initially wide DSD). Each point on the curves
499 corresponds to a certain time. Since the dependencies are plotted in non-dimensional
500 coordinates, the time instance $t = 0$ corresponds to coordinates (1, 1). The numbers along the
501 curves denote the points corresponding to time instance $t = 20\,\text{s}$. At lower RH_0, the curves reach
502 lower values of LWC and of droplet concentration. In case of an initially narrow DSD the curve
503 can be divided into three sections. The first section corresponds to high RH_0 ($RH_0 > 90\%$).

Within this section, the droplet concentration does not decrease with decreasing LWC, which is in line with the conceptual scheme of homogeneous mixing (Fig. 1). This section corresponds to the straight horizontal line in Fig. 8a. At lower relative humidity, the droplet concentration begins to decrease with a decreasing LWC, in line with Fig. 8a. When the LWC reaches small values, the dependence of the normalized LWC on the normalized droplet concentration becomes close to linear. At an initially wide DSD (Fig. 13b), the dependence of the LWC on droplet concentration is close to linear at all the values of RH_0. This linear dependence means that the mean volume radius varies only slightly during droplet evaporation.

It is noteworthy that all the curves plotted for different initial values of RH_0 coincide. This coincidence can be explained by the fact that all the DSDs used depend on four parameters, namely, the three parameters of the initial Gamma distribution and on $Q(t)$ (Eq. 31). The parameters of Gamma distributions are identical for each panel in Fig. 13. Parameter $Q(t)$ monotonically increases with time. At different RH_0, the values of $Q(t)$ reach the same values at different times. When the values of $Q(t)$ are the same, the DSDs and all the DSD moments are equal.

To sum up, at an initially narrow DSD and a comparatively large initial relative humidity $RH_0 > 87\%$ phenomenon demonstrates properties typically attributed to homogeneous mixing, when a decrease in both the LWC and the effective radius takes place at unchanged droplet concentration (Figs. 8a, 9b, 11a, 13a). In contrast, in the case of an initially wide DSD, the evolution of the DSD and its moments is close to that typically attributed to inhomogeneous mixing, when droplet evaporation leads to a decrease in LWC and in droplet concentration, while the effective radius remains unchanged. During the changes of a wide DSD, its shape remains similar to itself (Fig. 7b), which is also considered typical of inhomogeneous mixing.

5. Discussion: Application of the concept of homogeneous mixing in numerical modeling

The procedure of mixing in any cloud model involves two steps. At the first step, the changes in microphysical values in each grid point are calculated using the turbulent flux divergences. In case mixing takes place between any two volumes represented by neighbouring grid points, the mixing volume containing both grid points never becomes homogeneous (*a fortiori*, the microphysical values in these grid points do not become identical during one time step), so the spatial gradients of the microphysical variables remain between neighbouring grid points. This step represents inhomogeneous mixing at resolving scales. Mixing algorithm in models does not operate with "final" equilibrium values, as assumed in the classical mixing concepts, but rather with current time-dependent values. In contrast, the changes in the microphysical and thermodynamical variables in the volumes represented by one grid points are often considered uniform at each time step, and therefore, the modelled subgrid mixing is treated as homogeneous. Therefore, in most numerical models mixing is inhomogeneous at resolved scales, but homogeneous at subgrid scales.

The estimations in Tab. 1 indicate that mixing is homogeneous at scales lower than ~0.5 m. This means that to simulate homogeneous mixing explicitly, the grid spacing should be less than 0.5 m. If such grid spacing is used, the separation between mixing types could be described explicitly. However, grid spacing in most models significantly exceeds this value. This fact brings up two questions: "What error is introduced when the spatial scale separating mixing types in models is much larger than 0.5 m?" and "Why are spectral microphysics models with a resolution of 40-50 m able to reproduce observed DSD and their moments with high accuracy (Benmoshe et al., 2012; Khain et al., 2013, 2015; Magaritz-Ronen et al., 2014)?"

There are several factors that compensate errors in segregating mixing types in cloud models and allow using grid scale $L > L_{pr}$ with little effect on DSD. The first factor is that mixing leads

553 to formation of cloud zones characterized by a spatial correlation scale (radius of correlation) of
554 temperature, humidity and droplet concentration of about 150-250 m (Magaritz-Ronen et al.,
555 2014). Numerical experiments with Lagrangian-Eulerian model of Sc (Magaritz-Ronen et al.,
556 2014) have shown that the results are not sensitive to the choice of parcel size, if this size is
557 substantially smaller than the spatial radius of correlation. Therefore, the mixing type has a
558 minor effect on the results of mixing at scales lower than the radius of correlation.

559 The second factor is that in-cloud mixing often takes place at conditions close to saturation.
560 At such high humidity, homogeneous and inhomogeneous mixing yield practically the same
561 results. The similarity of results for the two mixing types is due to the fact that mixing in clouds
562 is not accompanied by an appreciable phase transition.

563 The third factor was pointed out by Hill et al. (2009), who explained that stratocumulus cloud
564 evolution is insensitive to the type of sub-grid mixing since the rates of condensation/evaporation
565 caused by the resolved dynamics are by two orders of magnitude greater than the
566 condensation/evaporation rate caused by the sub-grid processes.

567 The fourth factor that permits us to treat sub-grid mixing as homogeneous near cloud
568 interfaces is that DSDs are polydisperse, which is opposite what is assumed in the conventional
569 mixing considerations. In the present study it was shown that for a broad DSD, the changes of
570 r_{eff} remain small during mixing. So, a relatively small partial evaporation of droplets provide
571 sufficient amount of water vapor for saturation of the volume. In this case homogeneous mixing
572 becomes indistinguishable from inhomogeneous. The saturation of the volume may be facilitated
573 by entrainment of water vapor from neighboring cloud volumes.

574

575 **6. Conclusions**

576

577 The present study is focused on the dynamics of DSD transformation during the evaporation
578 stage of homogeneous mixing. The results can be summarized as follows.

579 1. Analytical equations describing time evolution of normalized supersaturation and
580 normalized LWC are obtained. It is found that these time dependences are universal functions
581 of a sole non-dimensional parameter $\gamma = 1 + \frac{S_{m0}}{A_2 q_{m0}}$. In particular, the dependences of normalized
582 LWC at the final stage on the cloud air fraction, used for plotting the universal mixing diagrams,
583 are obtained analytically. These diagrams also depend on a sole non-dimensional parameter
584 $R = \frac{S_2}{A_2 q_1} < 0$, which is proportional to supersaturation in dry volume and inversely proportional
585 to liquid water mixing ratio in a cloud volume. This parameter is uniquely related with parameter
586 γ by Eq. (24). It is shown that in many cases the major changes in the LWC take place during
587 the time period of the order of the phase relaxation time τ_{pr}. The equilibrium state can be
588 reached after several τ_{pr} periods.

589 2. It is shown that the phase relaxation time is a natural time scale of mixing process. This is
590 clearly seen from the universal renormalized evaporation equations, in which the phase
591 relaxation time plays the role of a time unit. In some studies (e.g. Baker and Latham, 1979;
592 Burnet and Brenguier, 2007; Andejchuk et al., 2009) evaporation time for an individual droplet
593 under given sub-saturation is considered as a characteristic time of mixing. The present study
594 shows that only the phase relaxation time should be used as the characteristic time scale of
595 mixing since we have to consider the behavior of a large amount of droplets. Supersaturation (or
596 sub-saturation) is not a parameter that determines the phase relaxation time. Thus, the utilization
597 of the evaporation time of individual droplet (at unchanged supersaturation) as the characteristic
598 time scale of mixing is physically ungrounded. A strict relationship between the changes in

599 supersaturation and in the liquid water mixing ratio makes it impossible to consider the changes
600 in an individual droplet size and in supersaturation independently.

601 3. An important outcome of this study is demonstration of a significant difference in the
602 evaporative behavior between narrow DSD and wide DSD. It is shown that homogeneous
603 evaporation of a wide DSD is accompanied by reduction in LWC and in droplet concentration
604 due to total evaporation of small droplets. Such changes of LWC and droplet concentration are
605 qualitatively different from those in the classic concept of homogeneous mixing. As a result,
606 homogeneous mixing may be erroneously interpreted as inhomogeneous one.

607 4. It is shown that the evolution of DSDs and their moments in case of polydisperse DSDs,
608 can qualitatively differ from that predicted by homogeneous mixing concept. Evaporation of a
609 comparatively wide DSD may even lead to an increase in the effective radii and DSD high
610 moments. This feature is typically attributed to inhomogeneous mixing.

611 Note that the role of DSD polydispersity in the mixing process is different from that in
612 diffusion droplet growth in ascending parcels. In an ascending adiabatic parcel the
613 supersaturation tends to zero with height, and the DSD width decreases with height as well. In
614 this case, it is possible to reproduce the height dependencies and the time dependencies of
615 supersaturation and of LWC using an "equivalent" monodisperse DSD with the same droplet
616 concentration as a polydisperse DSDs (Pinsky et al., 2014). As regards to mixing with a
617 polydisperse DSD, it cannot be reproduced using a monodisperse DSD, with a possible
618 exception in case of an initially extremely narrow DSD.

619

620 ***Acknowledgements.*** This research was supported by the Israel Science Foundation (grant
621 1393/14), the Office of Science (BER), the US Department of Energy Award DE-SC0006788
622 and the Binational US-Israel Science foundation (grant 2010446). Dr. Korolev's participation
623 was supported by Environment Canada.

624

625

626 **Appendix A: List of Symbols**

627

628 **Table A1 here**

629

630

631 **Appendix B. Derivation of closed equations for supersaturation and for liquid water**
632 **mixing ratio in the monodisperse DSD case.**

633

634 Let us consider motionless well-mixed adiabatic air volume having an initial supersaturation
635 $S_{m0} < 0$ and an initial liquid water mixing ratio q_{m0}.

636 1. Substitution of the formula of the liquid water mixing ratio $q = \frac{4\pi\rho_w}{3\rho_a} N r^3$ into the
637 equation for droplet radius evolution

638 $$r\frac{dr}{dt} = \frac{S}{F} \qquad \text{(B1)}$$

639 leads to the equation for the decrease of q with the time

640 $$\frac{dq}{dt} = \frac{3}{F}\left(\frac{4\pi\rho_w}{3\rho_a}\right)^{2/3} N^{2/3} S q^{1/3} = B N^{2/3} S q^{1/3} \qquad \text{(B2)}$$

641 where

642 $$B = \frac{3}{F}\left(\frac{4\pi\rho_w}{3\rho_a}\right)^{2/3} = const \qquad \text{(B3)}$$

643 2. Equation for supersaturation is written as (Korolev and Mazin, 2003)

644 $$\frac{1}{S+1}\frac{dS}{dt} = -A_2\frac{dq}{dt} \qquad \text{(B4)}$$

Integration of this equation under the assumption that $A_2 = const$ leads to the equation

$$\ln\left[S(t)+1\right] = -A_2 q(t) + C \qquad \text{(B5)}$$

where C is determined by initial conditions at $t = 0$

$$C = \ln(S_{m0}+1) + A_2 q_{m0} \qquad \text{(B6)}$$

Using Eqs. (B5) and (B6) one obtains the equation with respect to $S(t)$

$$S(t) = (S_{m0}+1)\exp\left\{-A_2\left[q(t)-q_{m0}\right]\right\} - 1 \qquad \text{(B7)}$$

3. Mutual substitution of Eqs. (B2) and (B7) leads to the closed differential equations for $q(t)$ and $S(t)$

$$\frac{dq}{dt} = BN^{2/3}\left[(S_{m0}+1)\exp\left\{-A_2(q-q_{m0})\right\} - 1\right]q^{1/3} \qquad \text{(B8)}$$

$$\frac{1}{S+1}\frac{dS}{dt} = -A_2 BN^{2/3} S\left(q_{m0} - \frac{1}{A_2}\ln\frac{S+1}{S_{m0}+1}\right)^{1/3} \qquad \text{(B9)}$$

Eqs. (B8) and (B9) should be solved with initial conditions $q(0) = q_{m0}$ and $S(0) = S_{m0}$ respectively.

4. In case $|S_{m0}| << 1$, supersaturation is close to zero all the time $|S(t)| << 1$ and Eqs. (B7-B9) can be simplified as follows

$$S(t) = S_{m0} - A_2\left[q(t) - q_{m0}\right] \qquad \text{(B10)}$$

$$\frac{dq}{dt} = -BN^{2/3}\left(A_2 q^{4/3} - (A_2 q_{m0} + S_{m0})q^{1/3}\right) \qquad \text{(B11)}$$

$$\frac{dS}{dt} = -B(A_2 N)^{2/3}(A_2 q_{m0} + S_{m0} - S)^{1/3} S \qquad \text{(B12)}$$

5. Then one can obtain Eqs. (B10-B12) in a non-dimensional form. Let us define time scale $\tau_{m0} = \left(BA_2 N^{2/3} q_{m0}^{1/3}\right)^{-1}$, normalized liquid water mixing ratio $\tilde{q} = \frac{q}{q_{m0}}$, normalized supersaturation

665 $\tilde{S} = \frac{S}{A_2 q_{m0}}$, and non-dimensional time $\tilde{t} = t / \tau_{m0} = BA_2 N^{2/3} q_{m0}^{1/3} t$. The Eqs. (B10-B12) can be

666 rewritten in a non-dimensional form as

667 $$\tilde{S}(\tilde{t}) = -\tilde{q}(\tilde{t}) + \gamma \qquad \text{(B13)}$$

668 $$\frac{d\tilde{q}}{d\tilde{t}} = \tilde{q}^{1/3}\left(\gamma - \tilde{q}\right) \qquad \text{(B14)}$$

669 $$\frac{d\tilde{S}}{d\tilde{t}} = -(\gamma - \tilde{S})^{1/3}\tilde{S} \qquad \text{(B15)}$$

670 where non-dimensional parameter $\gamma = 1 + \frac{S_{m0}}{A_2 q_{m0}}$ depends on initial supersaturation S_{m0} and

671 initial liquid water mixing ratio q_{m0}. Eq. (B14) should be solved with initial condition $\tilde{q}(0) = 1$

672 and Eq. (B15) should be solved with initial condition $\tilde{S}(0) = \frac{S_{m0}}{A_2 q_{m0}} < 0$. Note that Eqs. (B14) and

673 (B15) are rigidly connected by Eq. (B13).

674

675 **References**

676 Andejchuk, M., Grabowski, W. W., Malinowski, S. P., and Smolarkiewicz, P. K.: Numerical
677 simulation of cloud–clear air interfacial mixing: homogeneous vs. inhomogeneous mixing., *J.*
678 *Atmos. Sci.*, **66**, 2493–2500, 2009.

679 Anthes, R.A.,: Tropical cyclones-Their evolution, structure, and effects. Monograph 41,
680 Amer. Meteorol. Soc., 208 pp, 1982

681 Baker, M., and J. Latham: The evolution of droplet spectra and the rate of production of
682 embyonic raindrops in small cumulus clouds. *J. Atmos. Sci.*, **36,** 1612–1615, 1979.

683 Baker, M., R. G. Corbin, and J. Latham: The influence of entrainment on the evolution of
684 cloud drop spectra: I. A model of inhomogeneous mixing. *Quart. J. Roy. Meteor. Soc.*, **106,** 581–
685 598, 1980.

686 Baker M. B. and J. Latham: A diffusive model of the turbulent mixing of dry and cloudy air.
687 *Quart. J. R. Met.* Soc., **108**, 871-898, 1982

688 Bar-Or R. Z., I. Koren, O. Altaratz and E. Fredj: Radiative properties of humidified aerosol
689 in cloudy environment. *Atmos. Res.*, **118**, 280–294, 2012.

690 Benmoshe, N., M. Pinsky, A. Pokrovsky, and A. Khain: Turbulent effects on the
691 microphysics and initiation of warm rain in deep convective clouds: 2-D simulations by a
692 spectral mixed-phase microphysics cloud model. *J. Geophys. Res.*, **117**, 1–20, 2012.

693 Benmoshe N., M. Pinsky, A. Pokrovsky and A. Khain: Turbulent effects on microstructure
694 and precipitation of deep convective clouds as seen from simulations with a 2-D spectral
695 microphysics cloud model. *J. Geop. Res*., **117**, D06220, 2012.

696 Blyth, A. M., Choularton, T. W., Fullarton, G., Latham, J., Mill, C. S., Smith, M. H., and
697 Stromberg, I. M.: The Influence of entrainment on the evolution of cloud droplet spectra. 2. Field
698 experiments 5 at Great Dun Fell, *Q. J. Roy. Meteor. Soc*., **106**, 821–840, 1980.

699 Burnet, F., and J-L. Brenguier: Observational study of the entrainment-mixing process in
700 warm convective clouds. *J. Atmos. Sci.*, **64,** 1995–2011, 2007.

701 Denvich B. J., P. Bartello, J-L. Brenguier, L.R. Collins, W.W. Grabowski, R.H.A. Ijzermans,
702 S.P. Malinovski, M.W. Reeks, J.C. Vassilicos, L-P. Wang, and Z. Warhaft: Droplet growth in
703 warm turbulent clouds. *Q. J. Roy. Meteorol. Soc.*, **138**, 1401-1429, 2012.

704 Dimotakis P. E.: Turbulent mixing, *Annu. Rev. Fluid Mech*., **37**, 329-356, 2005.

705 Ferrier, B.S. and R.A. Houze: One-dimensional time dependent modeling of GATE
706 cumulonimbus convection. *J. Atmos. Sci.*, **46**, 330-352, 1989.

707 Gerber H, Frick G, Jensen J.B, and Hudson J.G.: Entrainment, mixing, and microphysics in
708 trade-wind cumulus. *J. Meteorol. Soc. Jpn.*, **86A**. 87-106, 2008.

709 Ghan S. J., Hayder Abdul-Razzak, A. Nenes, Yi Ming, Xiaohong Liu, M. Ovchinnikov, B.
710 Shipway, N. Meskhidze, Jun Xu and X. Shi: Droplet nucleation: Physically-based

711 parameterizations and comparative evaluation, *J. Adv. Model. Earth Syst*., 3, M10001, 33 pp.
712 DOI:10.1029/2011MS000074, 2011.

713 Goix P. J. and L. Talbot: Turbulent counter flow diffusion flame structure and dilution
714 effects combustion. *Science and Technology*, 79, #4-6, 1991.

715 Hill, A. A., G. Feingold, and H. Jiang: The influence of entrainment and mixing assumption
716 on aerosol–cloud interactions in marine stratocumulus. *J. Atmos. Sci.*, 66, 1450–1464, 2009.

717 Jeffery, C. A.: Inhomogeneous cloud evaporation, invariance, and Damköhler number. J.
718 Geophys. Res. 112, D24S21, doi:10.1029/2007JD008789

719 Kerstein A. R.: Linear eddy modelling of turbulent scalar transport and mixing, *Comb. Sci.*
720 *Technol*., 60, 391-421, 1988.

721 Kerstein A. R.: Linear-eddy modelling of turbulent transport. Part 6. Microstructure of
722 diffusive scalar mixing fields. *J. Fluid Mech*., **231**, 361-394, 1991.

723 Khain A., Thara V. Prabha, Nir Benmoshe, G. Pandithurai, M. Ovchinnikov: The mechanism
724 of first raindrops formation in deep convective clouds. *J. Geophys. Res.* Atmospheres**. 118**,
725 9123–9140, 2013.

726 Khain A.P. , K. D. Beheng, A. Heymsfield, A. Korolev, S.O. Krichak, Z. Levin, M. Pinsky,
727 V. Phillips, T. Prabhakaran, A. Teller, S.C. van den Heever, J.-I. Yano: Representation of
728 microphysical processes in cloud-resolving models: spectral (bin) microphysics vs. bulk
729 parameterization. *Review of Geophysics* (in press) , 2015

730 Knight C. A. and L. J. Miller: Early radar echoes from small, warm cumulus: Bragg and
731 hydrometeor scattering. *J. Atmos. Sci.*, **55**, 2974-2992, 1998.

732 Korn G. A. and T. M. Korn: Mathematical handbook for scientists and
733 engineers: Definitions, theorems, and formulas for reference and review. Courier Corporation –
734 Mathematics - 1130 pp, 2000.

Korolev, A.V.: The influence of suresaturation fluctuations on droplet size spectra formation. *J. Atmos. Sci.*, **52**, 3620-3634, 1995.

Korolev, A. V., and G. A. Isaac: Drop growth due to high supersaturation caused by isobaric mixing. *J. Atmos. Sci.*, **57,** 1675–1685, 2000.

Korolev A., V, Isaac, G. A.: Phase transformation of mixed-phase clouds. *Q. J. Roy. Meteorol. Soc*. **129**, 19-38, 2003.

Korolev, A. V., and I. P. Mazin: Supersaturation of water vapor in clouds. *J. Atmos. Sci.,* **60,** 2957–2974, 2003.

Korolev A., A. Khain, M. Pinsky, and J. French: Theoretical investigation of mixing in warm clouds. Part 1: Classical concept. Submitted, 2015

Kumar B, J. Schumacher, and R. A. Shaw: Cloud microphysical effects of turbulent mixing and entrainment. *Theor. Comput. Fluid Dyn*., **27**, 361–376, 2013.

Latham, J. and Reed, R. L.: Laboratory studies of effects of mixing on evolution of cloud droplet spectra, *Q. J. Roy. Meteor. Soc*., **103**, 297–306, 1977.

Lehmann, K., H. Siebert, R. A. Shaw: Homogeneous and inhomogeneous mixing in cumulus clouds: Dependence on local turbulence structure. *J. Atmos. Sci.*, **66**, 3641–3659, 2009.

Mazin, I. P.: Effect of phase transition on formation of temperature and humidity stratification in clouds. *Proc. Int. Conf. on Cloud Physics.* Toronto, Ontario, Canada, Amer. Meteor. Soc., 132– 137, 1968.

Magaritz-Ronen L., M. Pinsky, and A. Khain: Effects of turbulent mixing on the structure and macroscopic properties of stratocumulus clouds demonstrated by a Lagrangian trajectory model. *J. Atmos. Sci.,* **71**, 1843–1862, 2014.

Monin, A.S. and Yaglom, A.M.: "Statistical Fluid Mechanics: Mechanics of Turbulence", vol. **2**, MIT Press. 911 pp., 1975.

759 Pinsky, M. and A. P. Khain: Effects of in-cloud nucleation and turbulence on droplet
760 spectrum formation in cumulus clouds. *Quart. J. Roy. Meteorol. Soc*., **128**, 1–33, 2002.
761 Pinsky M., I.P. Mazin, A. Korolev, and A. Khain: Supersaturation and diffusional drop
762 growth in liquid clouds, *J. Atmos. Sci.*, **70**, 2778-2793, 2013.
763 Pinsky M., I. P. Mazin, A. Korolev and A. Khain: Supersaturation and diffusional droplet
764 growth in liquid clouds: Polydisperse spectra. *J. Geophys. Res., Atmospheres*, **119**, 12,872–
765 12,887, 2014
766 Pruppacher, H.R., Klett, J.D.: Microphysics of clouds and precipitation. 2nd edn. Oxford
767 Press, 914 p. , 1997
768 De Rooy, W. C., P. Bechtold, K. Fröhlich, C. Hohenegger, H. Jonker, D. Mironov, A. P.
769 Siebesma, J. Teixeira and J-I Yano: Entrainment and detrainment in cumulus convection: an
770 overview, *Q. J. Royal Met. Soc*., **139**, 1–19, 2013.
771 Stull, Roland B.: An Introduction to Boundary Layer Meteorology. Springer, Netherlands,
772 666 pp, 1988.
773 Troen, I. and L. Mahrt: A simple model of the atmospheric boundary layer: Sensitivity to
774 surface evaporation. *Boundary Layer Met.* **37**, 129-148, 1986.
775 Warhaft Z.: Passive scalars in turbulent flows. *Annu. Rev. Fluid Mech*., **32**, 203–240, 2000.
776 Warner J.: The microstructure of cumulus cloud. Part 1: general features of the droplet
777 spectrum, *J. Atmos. Sci.*, **26**, 1049-1059, 1969.
778
779

780

781 **Table 1.** Linear scales of volumes experiencing homogeneous mixing at conditions typical of

782 different cloud types.

Cloud type	N, cm^{-3}	LWC gm^{-3}	r, μm	Dissipation rate, cm^2/s^3	Phase relaxation time, s	Phase scale, m
Maritime Convective	100	2.0	16.8	300	2.01	0.49
Maritime Stratocumulus	100	0.5	10.6	10	3.19	0.18
Weak Stratocumulus	100	0.2	7.8	5	4.33	0.2
Continental Convective	500	2	8.0	500	0.75	0.6

783

784

785

786 **Table 2.** Estimations of mixing results at different environmental conditions*

T (^{o}C)	A_2	q_1, g/kg	RH_2 %	μ (cloud fraction)	$R\frac{1-\mu}{\mu}$	Result of mixing
$T = 0^oC$	400	1.0	95	0.5	-0.125	cloudy
$T = 0^oC$	400	1.0	50	0.5	-1.25	Non-cloudy
-10^oC	700	2.0	95	0.5	-0.036	cloudy
-10^oC	700	2.0	50	0.5	-0.36	cloudy
-20^oC	1500	2.0	95	0.5	-0.017	cloudy
-20^oC	1500	2.0	50	0.5	-0.17	cloudy
-20^oC	1500	2.0	95	0.1	-0.153	cloudy
-20^oC	1500	2.0	50	0.1	-1.53	Non-cloudy

787 * The values A_2 are estimated as proposed by Pinsky et al., (2013).

788

789

790 **Table 3.** Parameters of the initial Gamma distributions

DSD	N_{m0}, cm^3	α	β, μm	Modal radius, μm	LWC, g/m^3
Narrow	264.2	101.0	0.1	10.0	0.587
Wide	71.0	4.3	3.1	10.0	0.587

791

792

793

794 **Tab. A1. List of symbols**

795

Symbol	Description	Units
A_2	$\frac{1}{q_v}+\frac{L^2}{c_p R_v T^2}$, coefficient	nd
B	$\frac{3}{F}\left(\frac{4\pi\rho_w}{3\rho_a}\right)^{2/3}$, coefficient	$m^2\ s^{-1}$
C	constant of integration	nd
c_p	specific heat capacity of moist air at constant pressure	$J\ kg^{-1}K^{-1}$
$\mathscr{D}$	coefficient of water vapour diffusion in the air	$m^2\ s^{-1}$
e	water vapor pressure	$N\ m^{-2}$
e_S	saturation vapour pressure above a flat water surface	$N\ m^{-2}$
F	$F=\frac{\rho_w L^2}{k_a R_v T^2}+\frac{\rho_w R_v T}{e_S(T)\mathscr{D}}$, coefficient	$m^{-2}\ s$
$f(r,t)$	droplet size distribution	m^{-4}
$f_0(r_0)$	droplet size distribution after the first stage of mixing	m^{-4}
k_a	coefficient of air heat conductivity	$J\ m^{-1}s^{-1}K^{-1}$
L_{mix}	characteristic spatial scale of mixing	m
L_{pr}	spatial scale of phase relaxation	m
L	latent heat for liquid water	$J\ kg^{-1}$
N	droplet concentration	m^{-3}
N_1	droplet concentration in a cloud volume	m^{-3}
N_{m0}	droplet concentration after the first stage of mixing	m^{-3}
p	pressure of moist air	$N\ m^{-2}$
q	liquid water mixing ratio	kg/kg
q_1	liquid water mixing ratio in a cloudy volume	kg/kg
q_{m0}	liquid water mixing ratio after the first stage of mixing	kg/kg
q_w	liquid water content (LWC)	gm^{-3}

q_{w0}	LWC after the first stage of mixing	gm^{-3}
q_v	water vapor mixing ratio	kg/kg
$\tilde{q}$	normalised liquid water mixing ratio equal to normalized LWC	nd
$\tilde{q}_{\min}$	normalized equilibrium liquid water mixing ratio equal to normalized equilibrium LWC	nd
Q	change of square of droplet radius	m^2
r	droplet radius	m
R	$\frac{S_2}{A_2 q_1}$, potential evaporation parameter (PEP)	nd
R_a	specific gas constant of moist air	$J\ kg^{-1}K^{-1}$
R_v	specific gas constant of water vapor	$J\ kg^{-1}K^{-1}$
RH_0	$1+S_{m0}$, relative humidity after the first stage of mixing	nd
S	$e/e_w - 1$, supersaruration over water	nd
S_{m0}	supersaturation after the first stage of mixing	nd
S_2	supersaturation in a dry volume	nd
$\tilde{S}_{\max}$	maximal normalized supersaturation	nd
$\tilde{S}$	normalized supersaturation	nd
T	temperature	K
T_1	temperature in a cloud volume	K
T_2	temperature in a dry volume	K
t_e	normalized evaporation time	nd
t	time	s
$\tilde{t}$	non-dimensional time	nd
$x(\tilde{t})$	non-dimensional variable	nd
α	parameter of the Gamma distribution	nd
β	parameter of the Gamma distribution	m^{-1}
χ	$\gamma^{1/3}$, non-dimensional parameter	nd
ε	turbulent dissipation rate	m^2s^{-3}

γ	$1+\frac{S_{m0}}{A_2 q_{m0}}$, non-dimensional parameter	nd
δq_m	mixing ratio of liquid water required to saturate 1 kg of the cloud (or cloudy?) volume after instant mixing	nd
μ	mass fraction of cloud air	nd
ρ_a	air density	kg m^{-3}
ρ_w	density of liquid water	kg m^{-3}
τ_{pr}	phase relaxation time	s
τ_{mix}	characteristic time of mixing	s
τ_{m0}	time scale	s

"nd" denotes non-dimensional

Figures

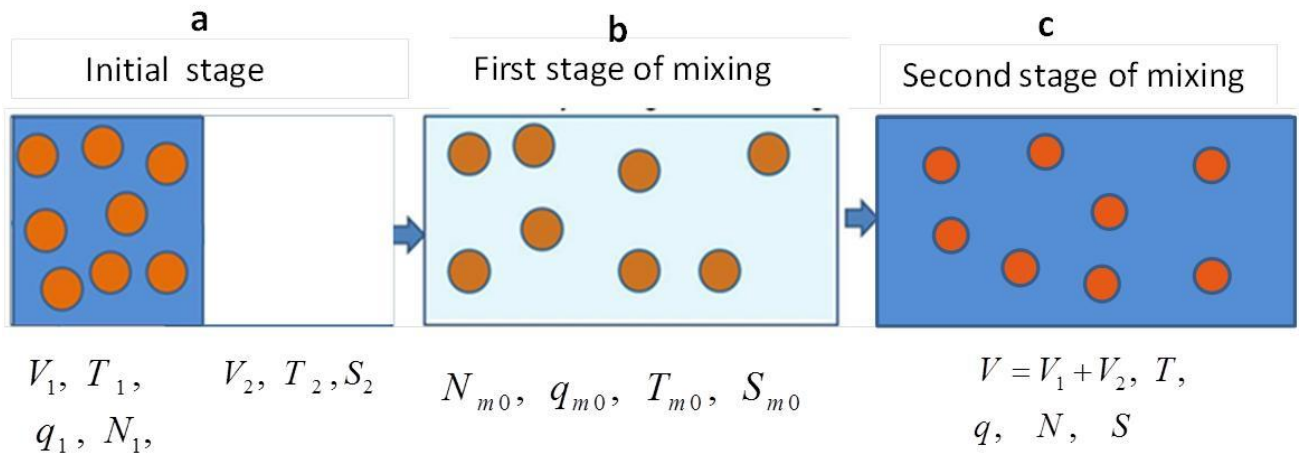

Fig. 1. Conceptual scheme of homogeneous mixing in case of monodisperse DSD. The subsaturated volume of dry air is colored white, and the cloudy volumes with saturated air are colored dark blue. The volume forming as a result of mixing after total homogenization is colored light blue. Index 1 shows the initial values characterizing the initially cloudy volume. Index 2 denotes initial values in the droplet-free volume. Index "$m0$" denotes values in the mixing volume after the first stage of mixing.

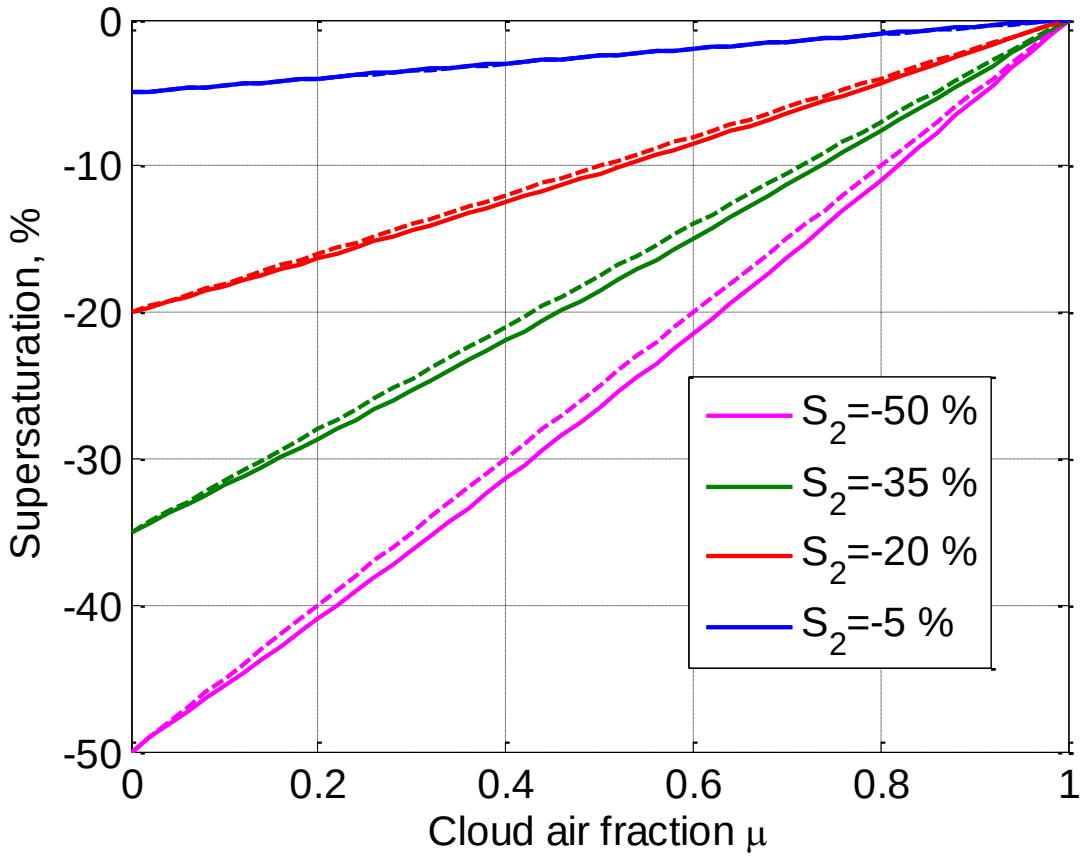

Fig. 2. Dependence of supersaturation on parameter μ: simulation results (solid line) and an approximate linear dependence calculated using Eq. (6b) (dashed line). The initial temperatures of two volumes are $T_1 = 8\,^{o}\mathrm{C}$ and $T_2 = 10\,^{o}\mathrm{C}$.

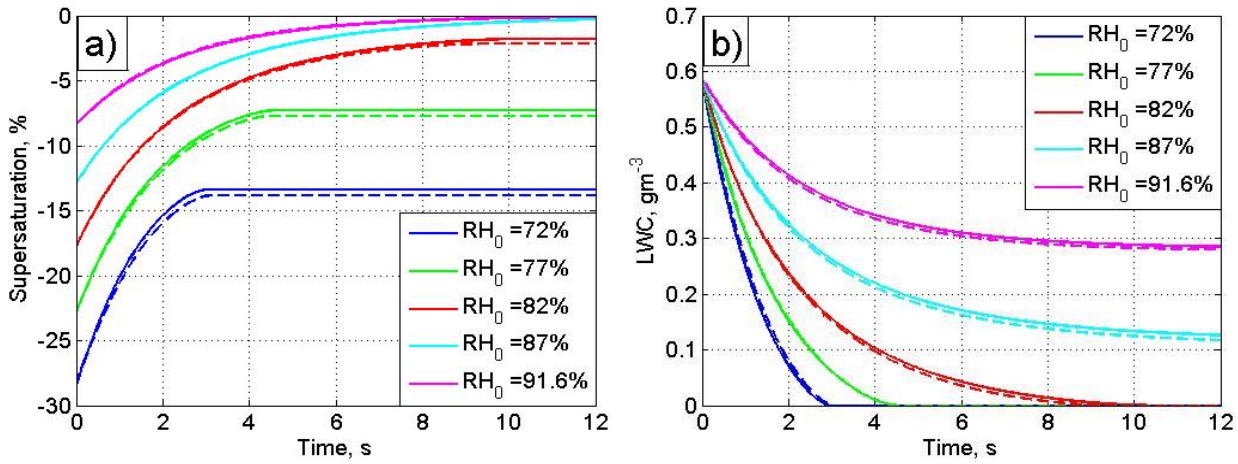

Fig. 3. Dependencies $S(t)$ (a) and $q_w(t)$ (b), calculated at different initial relative humidity RH_0 using closed differential equations (12,13) (solid lines) and using a parcel model (dashed lines). The calculation parameters are $T_{m0} = 10^{o}C$, $p_0 = 842$ mb, $r_0 = 10\ \mu m$, $N_{m0} = 140\ cm^{-3}$, $q_{w0} = 0.58\ gm^{-3}$.

884

885

886

887

888

889

890

891

892

893

894

895

896

897

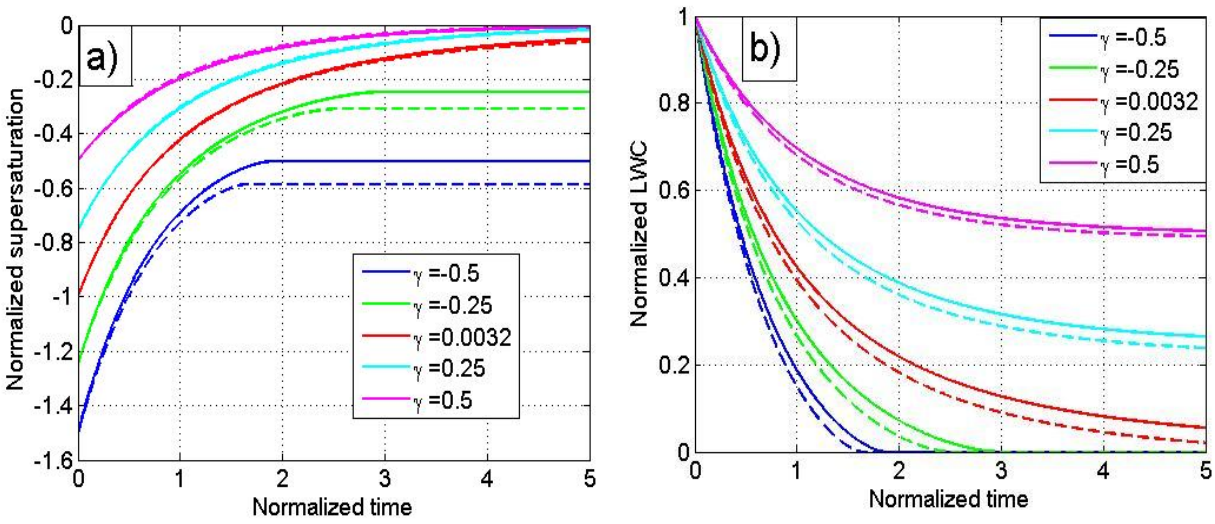

898

899

900 **Fig. 4.** Universal dependencies $\tilde{S}(\tilde{t})$ (a) and $\tilde{q}(\tilde{t})$ (b), calculated at different values of

901 parameter γ using Eqs. (17-18) (solid lines) and using a parcel model (dashed lines).

902

903

904

905

906

907

908

909

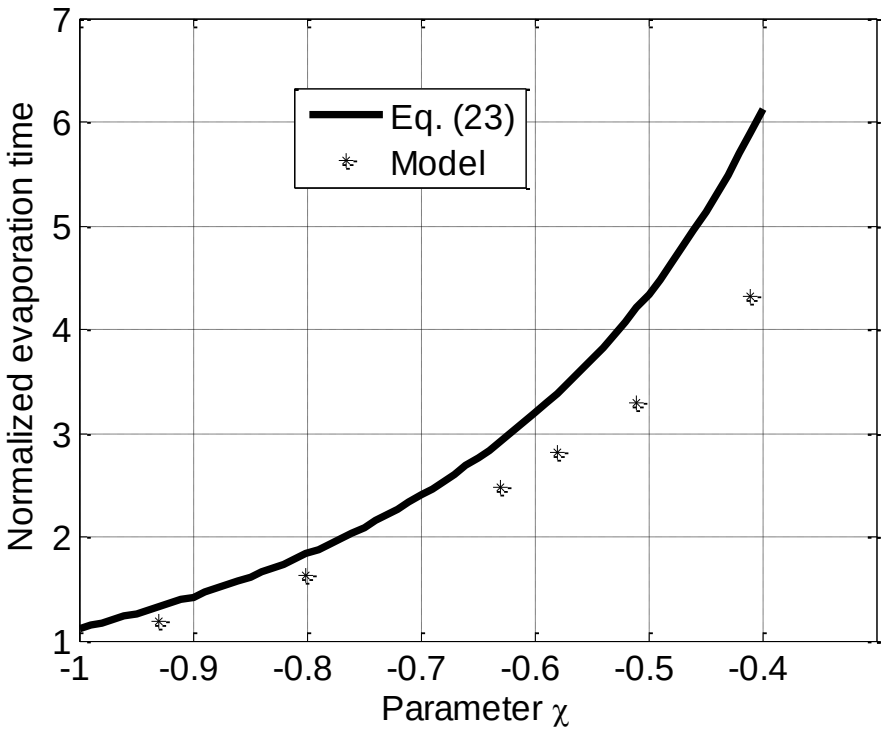

Fig. 5. Dependence of the evaporation time on parameter χ, $t_e(\chi)$. Time is measured at the relaxation time scales. The values obtained using a parcel model are shown by asterisks.

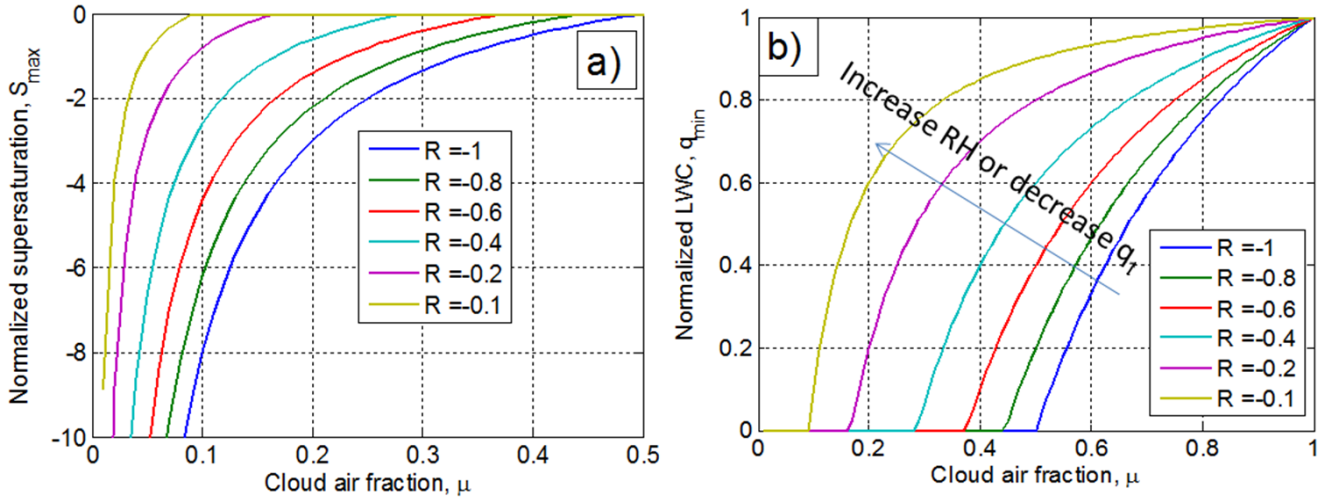

Fig. 6. Dependencies of normalized equilibrium supersaturation $\tilde{S}_{max}$ (a) and normalized equilibrium LWC (which is equal to normalized equilibrium liquid water mixing ratio) $\tilde{S}_{max}$ (b) on cloudy air fraction at the final stage of homogeneous mixing. Curves of different colors correspond to different values of non-dimensional parameter $R = \frac{S_2}{A_2 q_1}$.

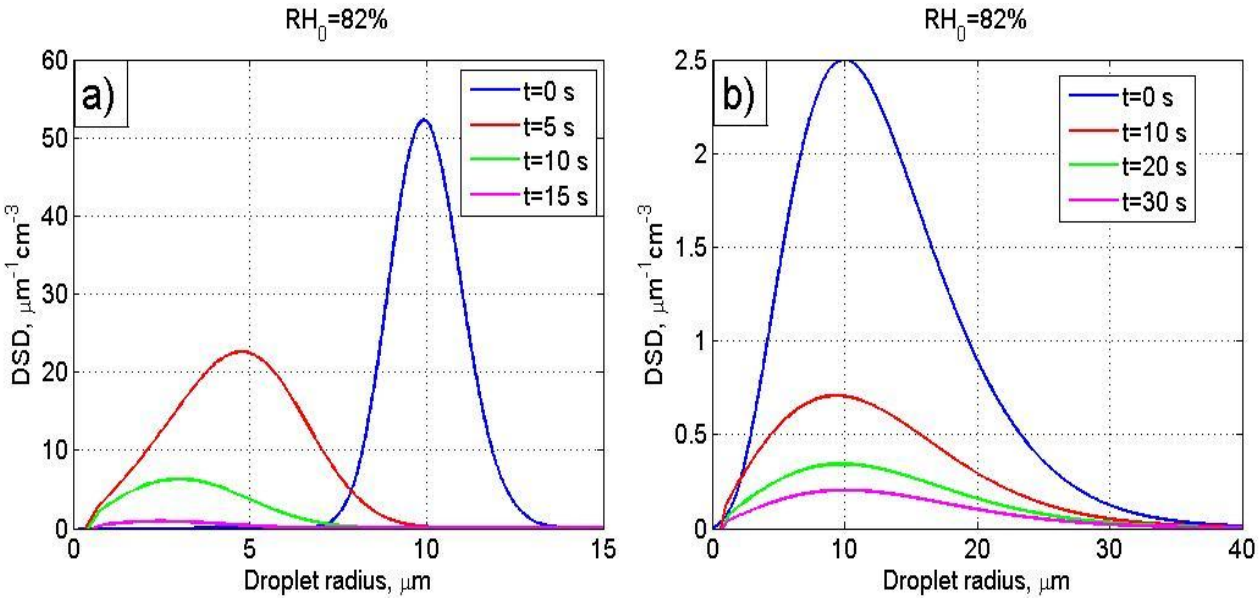

Fig. 7. Time evolution of an initially narrow DSD (a) and an initially wide DSD (b). The initial calculation parameters are the same in both examples: $T_{m0} = 10\ ^{o}C$, $p = 829$ mb, $RH_{m0} = 82\ \%$ and $q_{w0} = 0.587$ g/m^3. The parameters of the initial Gamma distributions are given in Tab. 3.

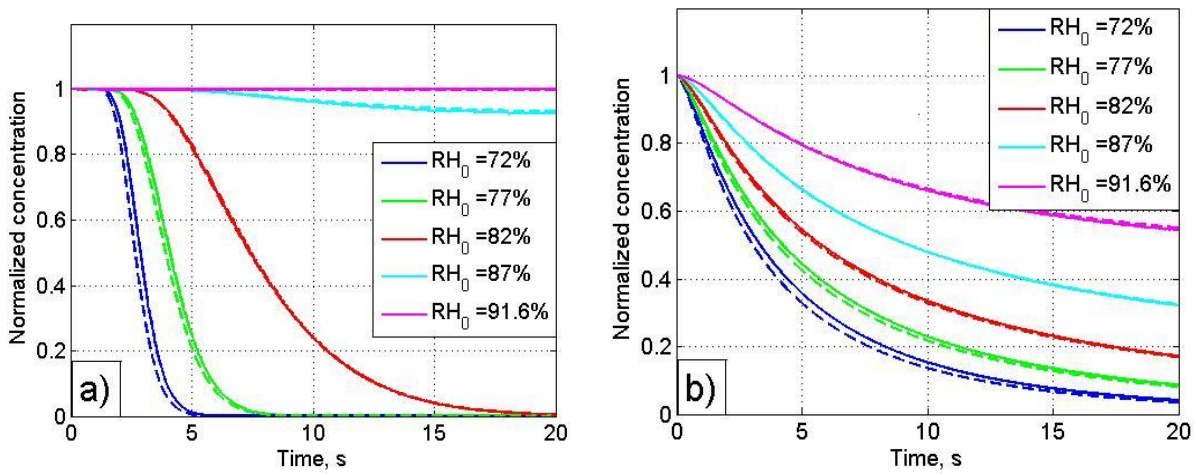

Fig.8. Time dependencies of normalized droplet concentration for an initially narrow DSD (a) and an initially wide DSD (b) at initially different values of RH_0 in the resulting volume. The dependencies are calculated directly using a parcel model (solid lines) and using Eq. (33) (dashed lines). The thermodynamic parameters are the same as in Fig.7. Parameters of the initial DSDs are given in Tab. 3.

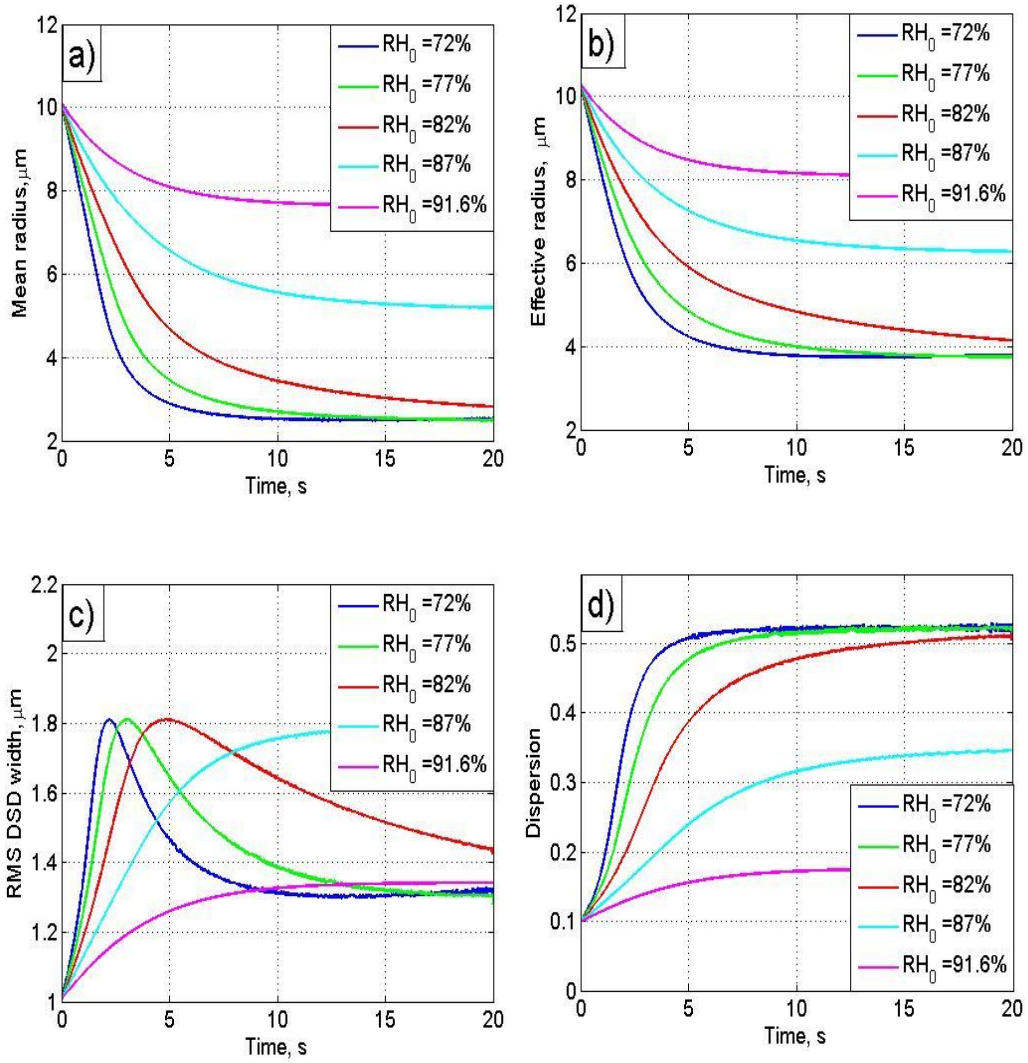

Fig. 9. Dependencies of moment functions typically used for characterizing DSD shape at different values of the initial relative humidity RH_0 in the resulting volume. The dependencies are calculated using a parcel model for an initially narrow DSD (Tab. 3). The thermodynamic parameters are the same as in Fig. 7.

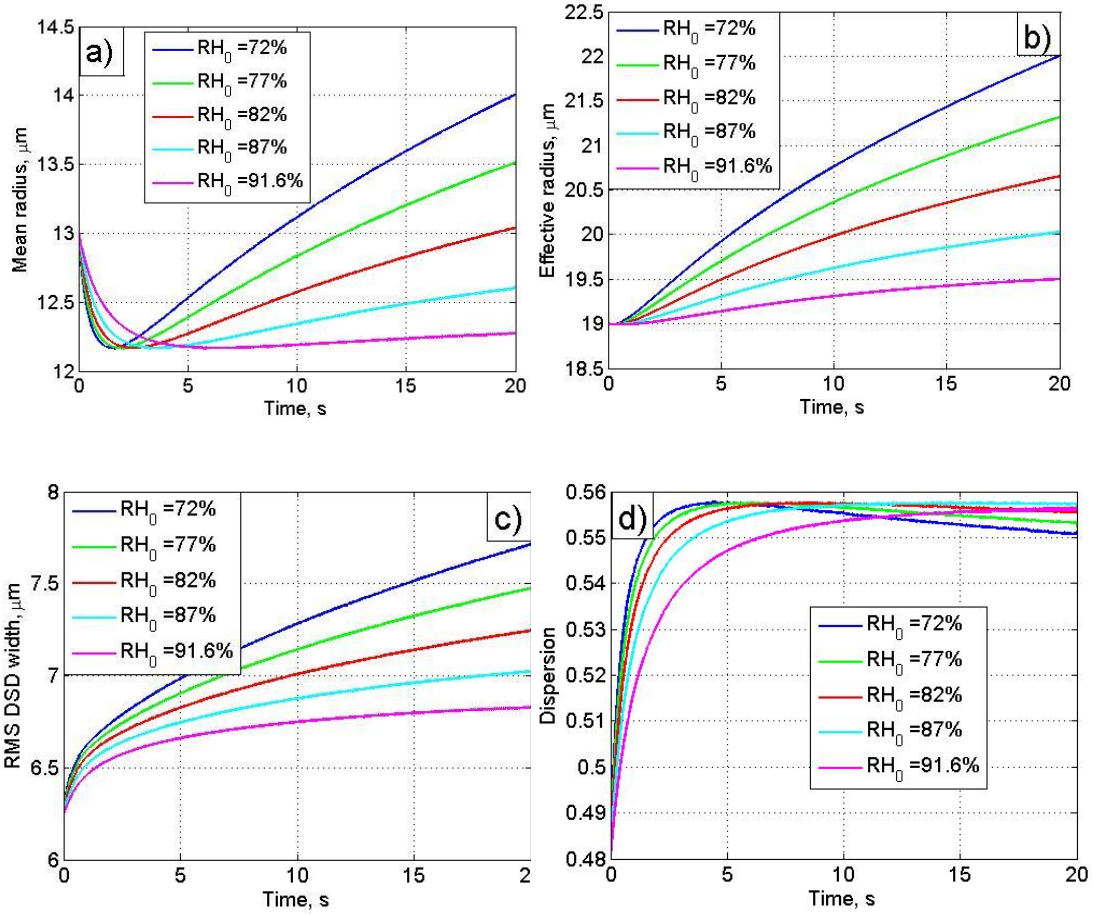

Fig. 10. The same as in Fig. 9 but for an initially wide DSD.

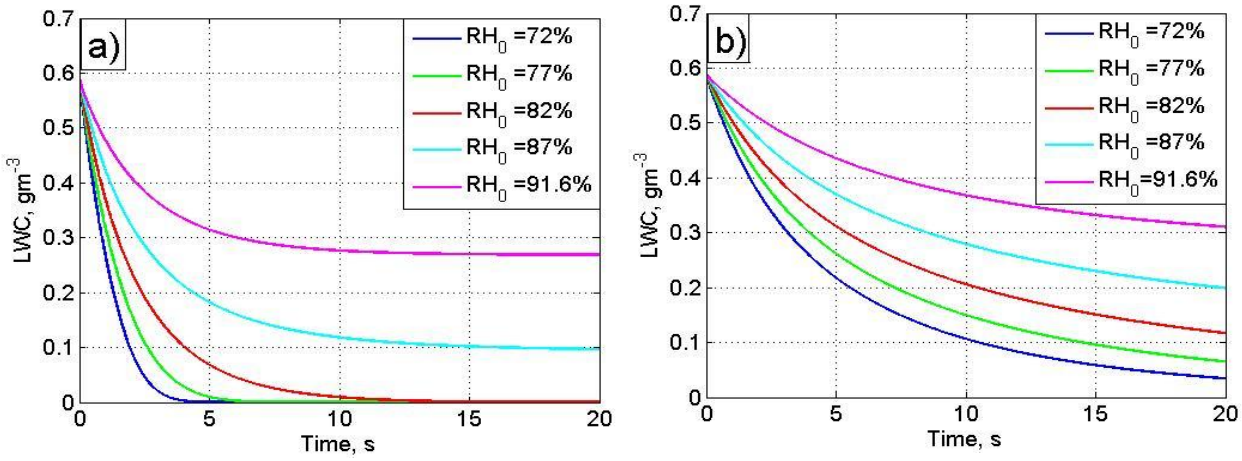

Fig. 11. Time dependencies of LWC calculated using a parcel model at different values of RH_0 in the resulting volume, for an initially narrow DSD (a) and an initially wide DSD (b). The thermodynamic parameters are the same as in Fig.7. The parameters of the initial DSDs are given in Tab. 3.

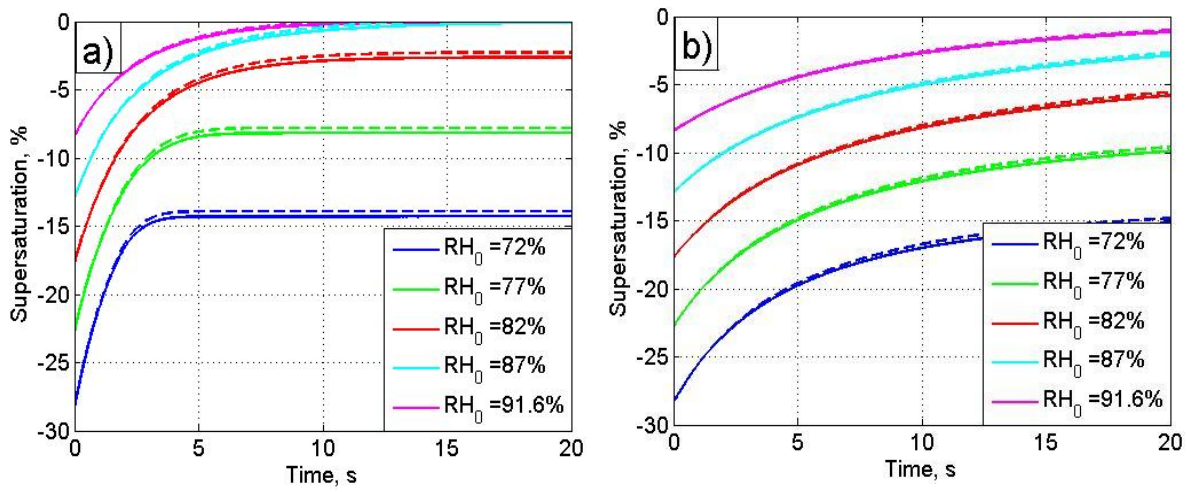

Fig. 12. Time dependencies of supersaturation calculated at different values of the initial relative humidity RH_0 in the resulting volume, using Eq. (8) (solid lines) and Eq. (40) (dashed lines), for an initially narrow DSD (a) and an initially wide DSD (b). The thermodynamic parameters are the same as in Fig.7. The parameters of the initial DSDs are given in Tab.3.

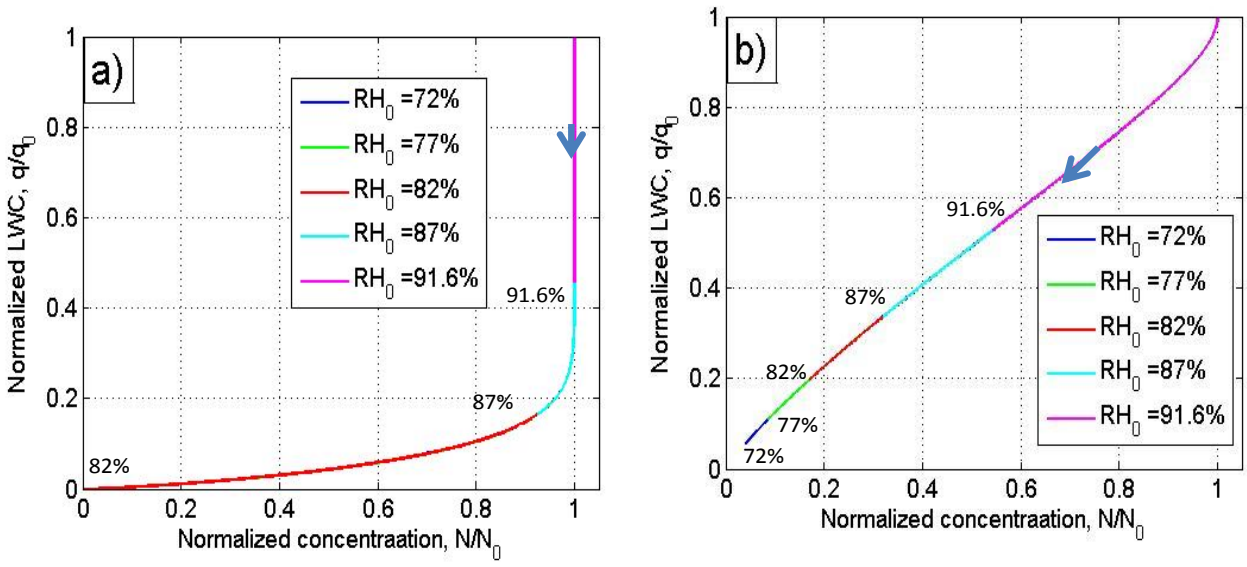

Fig. 13. Dependencies of normalized LWC on the normalized number concentration of droplets calculated at different values of the initial relative humidity RH_{m0} in the resulting volume, for an initially narrow DSD (a) and an initially wide DSD (b). The thermodynamic parameters are the same as in Fig.7. The parameters of the initial DSDs are given in Tab. 3. Arrows denote the direction of increasing time.